J. Fluid Mech. (2011), *vol.* 685, *pp.* 202–234.
doi:10.1017/jfm.2011.307

The rheology and microstructure of concentrated non-colloidal suspensions of deformable capsules

Jonathan R. Clausen‡, Daniel A. Reasor Jr and Cyrus K. Aidun†

G. W. Woodruff School of Mechanical Engineering, Georgia Institute of Technology, Atlanta, GA 30332, USA

(Received 11 November 2010; revised 3 May 2011; accepted 8 July 2011; first published online 23 September 2011)

A detailed study into the rheology and microstructure of dense suspensions of initially spherical capsules is presented, where capsules are composed of a fluid-filled interior surrounded by an elastic membrane. This study couples a lattice-Boltzmann fluid solver to a finite-element membrane model creating a robust and scalable method for the simulation of these suspensions. A Lees–Edwards boundary condition is used to simulate periodic simple shear to obtain bulk rheological properties, and three-dimensional results are presented for capsules in the regime of negligible inertia, Brownian motion and colloidal interparticle forces. The simulation results focus on describing the suspension rheology as a function of the particle concentration and deformability, and relating these macroscopic rheological findings to changes at the particle level, i.e. the suspension microstructure. Several important findings are made: suspensions of deformable capsules are found to be shear thinning, and the initially compressive normal stresses associated with rigid spherical suspensions undergo rapid changes with moderate levels of particle deformation. These normal stress changes are particularly evident in the first normal stress difference, which undergoes a sign change at fairly minor levels of deformation, and the particle pressure, which decreases rapidly with increasing particle deformability. Changes in the microstructure as quantified by the single-body microstructure and the pair distribution function are reported. Also, results calculating particle self-diffusion are presented and related to changes in the normal stresses.

Key words: capsule/cell dynamics, particle/fluid flow, suspensions

1. Introduction

Suspensions have long been of interest to researchers owing to their myriad of applications. Applications include biological systems (blood), the paper industry (wood fibre suspensions and coating flows), mining and petroleum industries (waste tailings and hydraulic fracturing) and home products (paints and cosmetics). Suspension flows are complex: even with a simple Newtonian suspending fluid, the presence of suspended particles creates non-Newtonian rheological effects. The behaviour of

† Email address for correspondence: cyrus.aidun@me.gatech.edu
‡ Present address: Sandia National Laboratories, Albuquerque, NM 87185, USA.

suspensions on macroscopic scales, i.e. length scales much larger than that of an individual particle, is strongly influenced by the shape and configuration of the suspended particles, referred to as the suspension microstructure. Whereas Newtonian fluids are composed of small molecules that relax towards an equilibrium configuration on time scales significantly smaller than those found in the macroscopic flow, suspensions are composed of particles whose configuration can be influenced by the macroscopic flow creating a non-equilibrium microstructure. The deviation from an equilibrium microstructure is related to the Péclet number, Pe, which quantifies the relative importance of flow to thermally driven diffusion (Brownian motion). The focus of this paper is on non-colloidal suspensions where $Pe \to \infty$, thus the suspension microstructure is strongly perturbed from equilibrium. The complex rheology exhibited by suspensions is in part driven by the non-equilibrium microstructure.

Early investigation into the behaviour of suspensions focused on the dilute regime for particles with simple shapes, e.g. spheres, ellipsoids and rods. For hard-sphere suspensions, Einstein (1906, 1911) derived the dilute-limit effect of volume concentration on the suspension viscosity, and Batchelor & Green (1972) extended this analysis to two-body interactions; however, analytical work becomes intractable when many-body interactions must be included, since a detailed description of the microstructure is required. Analytical descriptions also exist for dilute suspensions of high-aspect-ratio particles (Batchelor 1970; Hinch & Leal 1972, 1973). For dense rigid-sphere suspensions, numerical techniques have proven invaluable in elucidating the connection between microstructure and rheology. Through Stokesian dynamics (SD) simulations (e.g. Brady & Bossis 1988; Phung, Brady & Bossis 1996; Sierou & Brady 2002), suspensions of non-colloidal rigid spheres have been studied extensively. These simulations have revealed asymmetric particle configurations, as well as non-Newtonian rheology including normal stress differences. Experimentally, the asymmetric particle configuration has been observed (Parsi & Gadala-Maria 1987), and non-Newtonian rheology has been reported (Zarraga, Hill & Leighton 2000; Singh & Nott 2003).

Introducing deformation to the suspended particles creates a more complicated system whose rheology differs from the rigid-sphere case. For example, suspensions of droplets exhibit deformation-induced shear thinning and a positive rather than negative first normal stress difference (Loewenberg & Hinch 1996; Zinchenko & Davis 2002). Although these effects may also be seen in rigid-particle suspensions, they are present at dilute concentrations in deformable-particle suspensions. Early investigation into the rheology of suspensions of deformable particles was undertaken by Taylor (1932), who extended the viscosity calculation of Einstein to droplets, and by Goddard & Miller (1967) and Roscoe (1967), who studied the rheology of dilute suspensions of viscoelastic particles. Two commonly studied deformable particles, capsules and vesicles, both consist of a fluid-filled interior surrounded by a membrane; however, a distinction needs to be made: capsules are surrounded by an elastic membrane, which may support bending moments, whereas a vesicle's membrane strongly resists area dilatation and usually supports bending moments. Consequently, vesicles need to be non-spherical in their equilibrium configuration, while capsules may or may not be spherical in their equilibrium configuration.

Early analytical work on the dynamics of isolated capsules used a perturbation analysis about a spherical shape (Barthès-Biesel 1980), and analytical work has progressed considerably in describing the dynamics and dilute-limit rheology for both capsules and vesicles. Analysis has explored the complex and nonlinear dynamical behaviour of capsules and vesicles, in which the major dynamical modes of capsules

and vesicles are tank treading, tumbling (Keller & Skalak 1982; Vlahovska & Gracia 2007), and vacillating breathing (or swinging) (Misbah 2006). In the tank-treading mode, the particle obtains an ellipsoidal configuration about which the membrane rotates in a motion similar to the treads of a tank, in the tumbling mode, the tank-treading behaviour is superposed onto a rigid-body tumbling motion, and in the vacillating breathing mode, the vesicle orientation oscillates relative to the flow direction while the particle's major and minor axes undergo a breathing mode oscillation. The transition between different regimes is highly dependent on particle shape (reduced area), membrane constitutive model and the viscosity contrast between internal and external fluids. Purely elastic membranes that are not capable of supporting bending moments have been found to demonstrate a buckling instability in the tank-treading configuration (Lac *et al.* 2004; Barthès-Biesel 2009). The dilute limit rheology has also been explored via analytical analysis for capsules (Barthès-Biesel & Rallison 1981) and vesicles (Misbah 2006; Vlahovska & Gracia 2007) and the major findings have been supported by extensive numerical simulation, (Ramanujan & Pozrikidis 1998; Biben & Misbah 2003; Bagchi & Kalluri 2010; Ghigliotti, Biben & Misbah 2010; Clausen & Aidun 2010).

In the dilute limit, suspensions of deformable particles are shear thinning due to the increased deformation of the suspended phase. Unlike dilute rigid-sphere suspensions, deformable-particle suspensions are capable of creating non-Newtonian normal stresses. A rheological feature of both capsules and vesicle suspensions is the presence of a minimum in shear viscosity as a function of the viscosity ratio between inner and suspending fluids. In vesicles, this minimum corresponds to the transition point between tank-treading and tumbling behaviours (Danker & Misbah 2007); however, recent numerical simulations of elastic capsules in a tank-treading configuration also demonstrate a minimum that is not attributable to a transition in dynamics (Bagchi & Kalluri 2010). It is also important to note that droplets and vesicles show qualitative differences in their dilute-limit rheology (Ghigliotti *et al.* 2010): droplets show an increasing suspension shear viscosity as the viscosity contrast increases, whereas vesicles show the opposite trend in the tank-treading regime.

Analytical extension of dilute-limit capsule or vesicle results to concentrated suspensions encounter the same difficulties as in rigid hard-sphere suspensions. Most existing numerical techniques are too computationally demanding to scale to a large enough number of particles to obtain accurate rheological results, thus, a numerical technique has been developed that couples the lattice-Boltzmann (LB) technique for suspensions (Aidun & Lu 1995; Aidun, Lu & Ding 1998) to a finite-element (FE) description of the capsule membrane to obtain information on the microstructure and rheology of capsule suspensions (MacMeccan *et al.* 2009). The LB/FE method developed does have several disadvantages. First, owing to the linearity of the FE model, capsule deformations are limited to relatively modest levels. Second, and perhaps most restrictive, the body-fixed coordinate system discussed in § 3.2, which is used to create invariant FE matrices to allow for efficient computation of the particle dynamics, does not capture proper tank-treading behaviour except for the case of an initially spherical capsule. The FE method can be replaced with more advanced methods for resolving the membrane mechanics and particle motion, such as the spectrin-link method (Reasor, Clausen & Aidun 2011), without adding significantly to the computational time. The LB/FE method has several strengths; however, such as the ability to scale on massively parallel computers (Clausen, Reasor & Aidun 2010), the ability to simulate finite-Reynolds-number flows, and the ability to handle viscosity contrast. The authors note that several other groups have successfully used the LB

method to simulate large numbers of deformable particles in both two (Bagchi 2007; Zhang, Johnson & Popel 2007) and three dimensions (Dupin *et al.* 2007).

In light of the limitations of the current LB/FE method and the rather large parameter space available, efforts will be focused on non-colloidal, initially spherical capsules with the same internal and external fluid, i.e. no viscosity contrast. This system represents the simplest departure from hard-sphere rigid particles to elastic capsules, and is a good starting point for the investigation of dense suspensions of deformable particles involving membranes (capsules and vesicles). The authors note that the use of initially spherical capsules precludes the investigation into rheological changes driven by changes in the particle dynamical regime (tank treading, tumbling, vacillating breathing). The authors are not aware of any other simulations that resolve the rheology of dense suspensions of elastic capsules in three-dimensions including the full particle-phase stress tensor. Efforts are made to relate the observed rheology to changes in the microstructure. In contrast to spherical particles that have no preferential alignment, the accurate description of the microstructure of capsule suspensions must also account for the single-body microstructure, i.e. the orientation of the capsule with respect to the flow direction and the relative deformation, in addition to the configurational microstructure seen with spherical particles. Also, particle self-diffusion results are shown for the highest concentration case and related to changes in the particle normal stresses.

2. Relevant parameters and governing equations

In this paper, we restrict ourselves to suspensions of initially spherical capsules undergoing simple shear in a Newtonian fluid, in which both inertial effects and Brownian motion are negligible. Assumptions of negligible inertia and Brownian motion are reasonable in many applications, for example blood flow, in which the particle size is of the order of 10 μm. The influence of inertia on the particle scale is quantified by the particle Reynolds number, which for linear shear is defined as $Re_p = \rho\dot{\gamma}a^2/\mu$, where ρ is the fluid density, $\dot{\gamma}$ is the shear rate, a is the particle radius and μ is the suspending fluid viscosity. As mentioned in the introduction, the influence of Brownian motion is quantified by the Péclet number, defined as $Pe = 6\pi\mu\dot{\gamma}a^3/k_BT$, where k_B is Boltzmann's constant and T is the temperature. For the case of negligible inertia and negligible thermal motion, $Re_p = 0$ and $Pe \to \infty$. For elastic capsules, the capillary number describes the relative influence of viscous to elastic stresses, which is defined as $Ca_G = \mu\dot{\gamma}a/G_M$, where G_M is the membrane shear modulus. This capillary number is analogous to that of droplets, except membrane forces are elastic in nature rather than driven by surface tension effects. The membrane shear modulus is related to the material shear modulus through $G_M = G_s t_m$, where t_m is the thickness of the membrane. For membranes capable of supporting bending moments, the reduced bending ratio quantifies the relative importance of bending to shear stresses and is defined as $E_b = \kappa_b/a^2E_y t_m$, where κ_b is the bending modulus of the material, and E_y is the Young's modulus of the material. The capsules simulated are stress-free in their equilibrium spherical shape.

First, we define a simulation domain Ω into which elastic capsules are embedded with the capsule membrane denoted by Ω_p. Note that the capsule membrane is of finite volume, and the membrane fluid–solid interface, both internal and external, is given by Γ. If a distinction between external and internal fluid–solid interfaces is required, it will be denoted by the superscripts (0) and (1) for variables on the external and internal surfaces, respectively. Neglecting inertia and assuming the interior

and exterior fluids have the same densities, the governing equations for the fluid phase are the Stokes and continuity equations, defined along with the Newtonian constitutive relation for the fluid stress as

$$\boldsymbol{\nabla} \cdot \boldsymbol{\sigma}_f = 0 \quad \text{in } \Omega \setminus \Omega_p, \tag{2.1a}$$

$$\boldsymbol{\nabla} \cdot \boldsymbol{u} = 0 \quad \text{in } \Omega \setminus \Omega_p, \tag{2.1b}$$

$$\boldsymbol{\sigma}_f = -p\boldsymbol{I} + \mu(\boldsymbol{\nabla u} + \boldsymbol{\nabla u}^{\mathrm{T}}), \tag{2.1c}$$

where $\boldsymbol{I}$ is the identity tensor, p is the fluid pressure and $\boldsymbol{u}$ is the fluid velocity. The membrane is treated as having a finite thickness, thus the governing equation is Cauchy's momentum equation and Hooke's law is used for the solid stress constitutive equation, shown as

$$\boldsymbol{\nabla} \cdot \boldsymbol{\sigma}_p = 0 \quad \text{in } \Omega_p, \tag{2.2a}$$

$$\boldsymbol{\sigma}_p = \lambda \,\mathrm{tr}(\boldsymbol{\nabla x})\boldsymbol{I} + G_s(\boldsymbol{\nabla x} + \boldsymbol{\nabla x}^{\mathrm{T}}), \tag{2.2b}$$

where $\boldsymbol{x}$ is a material point on the solid surface; λ and G_s are the Lamé constants that are readily related to other material parameters such as Young's modulus and the Poisson ratio. These equations are augmented by kinematic and dynamic boundary conditions at the fluid-membrane interface such that

$$\boldsymbol{u} = \frac{\mathrm{d}\boldsymbol{x}}{\mathrm{d}t} \quad \text{on } \Gamma, \tag{2.3a}$$

$$\boldsymbol{\sigma}_f \cdot \boldsymbol{n} = \boldsymbol{\sigma}_p \cdot \boldsymbol{n} \quad \text{on } \Gamma, \tag{2.3b}$$

where $\boldsymbol{n}$ is the normal vector pointing away from the solid membrane. The finite thickness of the membrane combined with the Hookean-elastic constitutive model results in a membrane that resists shear, area dilatation and bending forces. For the calculation of bulk rheology, the domain Ω should be infinite; however, this is not practical in numerical simulations, necessitating the use of a finite-sized periodic domain that still allows the imposition of shear.

Determination of suspension rheology is achieved by using the average-stress formulation as outlined by Batchelor (1970). Using angled brackets to denote averages, the stress in a suspension can be split into two portions, shown as

$$\langle \boldsymbol{\Sigma} \rangle = \langle \boldsymbol{\Sigma}^f \rangle + \langle \boldsymbol{\Sigma}^p \rangle, \tag{2.4}$$

where $\langle \boldsymbol{\Sigma}^f \rangle$ represents the average stress that would be present in the fluid in the absence of all particles (up to an arbitrary isotropic contribution), and $\langle \boldsymbol{\Sigma}^p \rangle$ represents the alteration in stress due to the presence of the particles. Assuming a Newtonian suspending fluid, $\langle \boldsymbol{\Sigma}^f \rangle = -P_f\boldsymbol{I} + 2\mu\langle \boldsymbol{E} \rangle$, where P_f is the average pressure within this fluid phase ($P_f = \langle p \rangle_f$), $\boldsymbol{I}$ is the identity tensor and $\boldsymbol{E}$ is the rate-of-strain tensor. Rigorously, the averages used above are ensemble averages over the probability space of all particle configurations; however, for linear shear flow the average stress field is homogeneous, thus a volume average is appropriate. Assuming negligible inertia, the particle contribution to the suspension stress can be calculated using the stresslet formulation (Batchelor 1970),

$$\begin{aligned}\langle \boldsymbol{\Sigma}^p \rangle &= \frac{1}{V}\sum_{i=1}^{N} \boldsymbol{S} \\ &= \frac{1}{V}\sum_{i=1}^{N} \int_{A_i} \left\{ \frac{1}{2}((\boldsymbol{\sigma}_f^{(0)} + P_f\boldsymbol{I}) \cdot \boldsymbol{nr} + \boldsymbol{r}(\boldsymbol{\sigma}_f^{(0)} + P_f\boldsymbol{I}) \cdot \boldsymbol{n}) - \mu(\boldsymbol{un} + \boldsymbol{nu}) \right\} \mathrm{d}A_i, \end{aligned} \tag{2.5}$$

where $\boldsymbol{r}$ is the position vector, V is the domain volume, N is the number of particles, $\boldsymbol{n}$ is the surface normal and the integration is performed over the external surface of the ith particle.

Some subtleties in the formulation of (2.4) and (2.5) need to be highlighted, specifically with regards to the application to capsules. In (2.5), the first term in the integral represents the symmetric portion of the first moment of the *external* traction vectors on the surface of the membrane due to hydrodynamic or other interparticle interaction forces. These traction vectors have been adjusted such that they represent the forces over those that would be present because of a mean fluid pressure. This adjustment for the mean pressure is required since P_f has already been included in $\langle \boldsymbol{\Sigma}^f \rangle$. The second term within the integral accounts for the viscous fluid stresses that were already included in $\langle \boldsymbol{\Sigma}^f \rangle$. This highlights an important difference compared with rigid-sphere suspensions: for a rigid particle the last term in the integral in (2.5) vanishes, thus $\langle \boldsymbol{\Sigma}^f \rangle$ is the average stress in the fluid; however, a capsule undergoes a straining motion, thus $\langle \boldsymbol{\Sigma}^f \rangle$ represents the average stress in the fluid in the absence of particles, or alternately, the stress due to the imposed strain. The true average stress in the fluid accounting for the perturbed flow caused by the particles is coupled to the straining motion in the solid since $\langle \boldsymbol{E} \rangle = \langle \boldsymbol{E}^f \rangle + \langle \boldsymbol{E}^p \rangle$.

An alternate, but equivalent, form of (2.5) is frequently used when dealing with capsules (Kennedy, Pozrikidis & Skalak 1994), in which the membrane is treated as infinitely thin, and the particle stress is posed in terms of a jump condition in the stress across the membrane. In this case, the stress of the internal fluid must be explicitly included, shown as

$$\langle \boldsymbol{\Sigma}^p \rangle = \frac{1}{V} \sum_{i=1}^{N} \int_{A_i} \left\{ \frac{1}{2} (\Delta \boldsymbol{f} \boldsymbol{r} + \boldsymbol{r} \Delta \boldsymbol{f}) - \mu (1 - \lambda_\mu)(\boldsymbol{u}\boldsymbol{n} + \boldsymbol{n}\boldsymbol{u}) \right\} \mathrm{d}A_i, \tag{2.6}$$

where $\Delta \boldsymbol{f} = (\boldsymbol{\sigma}_f^{(0)} - \boldsymbol{\sigma}_f^{(1)}) \cdot \boldsymbol{n}$, $\lambda_\mu = \mu^{(1)}/\mu^{(0)}$. The last term accounts for the additional stresses generated by the straining of the internal fluid over the stresses that would be generated had the particle not been present. In the special case of $\lambda_\mu = 1$, the viscous stresses generated by the straining motion internal to the particle are exactly balanced by the straining in the fluid outside the particle dictated by the volume-averaged rate of strain. In other words, the viscous stresses generated within the capsule do not affect the bulk stress, although viscous stresses are certainly present even in the case of $\lambda_\mu = 1$. In the form of (2.5), the internal viscous stresses would be captured in the increased forces acting externally to the particle. We also note that (2.6) does not contain the appropriate corrections to properly resolve the isotropic stress contribution in the case that $P_f \neq 0$.

From this average-stress formulation, rheological parameters can be readily calculated including the relative shear viscosity, $\mu_r = \Sigma_{12}/(\mu\dot{\gamma})$, the first normal stress difference, $N_1 = \Sigma_{11} - \Sigma_{22}$, and the second normal stress difference, $N_2 = \Sigma_{22} - \Sigma_{33}$. The stress tensor components are defined according the right-handed basis vectors $\boldsymbol{\delta}_1$, $\boldsymbol{\delta}_2$, and $\boldsymbol{\delta}_3$ which correspond to the flow, shear and vorticity directions, respectively. In contrast to the research of Batchelor (1970) and other early investigations, recent research has highlighted the importance of the isotropic portion of the particle stress, i.e. the particle pressure, which is defined as $\Pi_p = -1/3\,\mathrm{tr}(\boldsymbol{\Sigma}^p)$ (Jeffrey, Morris & Brady 1993). At first glance, the isotropic portion of the stress would appear to be inconsequential owing to the incompressibility of both fluid and solid phases. Since Π_p represents the deviation of the suspension pressure from the mean fluid pressure and is independent of the selection of P_f, P_f is an arbitrary quantity that can be set

to satisfy the far-field boundary conditions. Assuming a far-field pressure of zero, one can easily see that (2.4) requires a balance between the fluid and particle stresses such that $P_f = -\Pi_p$. The proper description of the individual normal stresses including the isotropic pressure term is critical to describing particle migration using the suspension balance formulation (Nott & Brady 1994), in which the relative migration of the particles is driven by gradients in the particle-phase stress. The suspension balance model has been successful in describing particle motion in many situations including curvilinear flows (Morris & Boulay 1999) and viscous resuspension (Morris & Brady 1998). A detailed discussion of the particle pressure and its relationship to osmotic pressure and particle migration and diffusion can be found in Yurkovetsky & Morris (2008). Any progress towards describing the migration of deformable particles in dense suspensions using the suspension balance model requires an accurate description of the normal stresses. The authors note that for deformable particles, migration due to wall effects (Karnis & Mason 1967; Sukumaran & Seifert 2001) and nonlinear shear fields (Coupier *et al.* 2008; Kaoui *et al.* 2008) must be considered in conjunction with normal-stress driven migration.

The rheological behaviour is dictated by the structure of the suspended phase on the particle length scale (microstructure). In suspensions of rigid spheres, the structure is entirely described by the configuration of all particles relative to one another; the symmetry inherent to the spherical shape precludes the creation of any single-body microstructure. The configurational microstructure is quantified through the pair distribution function, $g(\boldsymbol{r})$, which describes the probability of finding another particle centred at position $\boldsymbol{r}$ relative to a particle located at the origin, where the probability has been normalized by the number concentration of particles (Morris & Katyal 2002). In the purely hydrodynamic limit, pairwise interactions of non-colloidal spheres display fore–aft symmetry owing to the reversibility of Stokes flow, and thus dilute mixtures have symmetric pair distribution functions. On the macroscale, this symmetry results in Newtonian flow behaviour. In dense suspensions, however, reversibility is destroyed, and a noticeable asymmetry is seen (Gadala-Maria 1979). This asymmetry in the particle configuration, which is caused by interparticle interactions and the chaotic motion of particles as they interact hydrodynamically, gives rise to non-Newtonian flow behaviour (Brady & Morris 1997; Morris & Katyal 2002).

For suspensions of orientable particles, which include suspensions of droplets, rods, polymers or elastic capsules, the single-body microstructure becomes a relevant parameter in addition to the relative positions of the particles with respect to one another. In the case of tank-treading elastic capsules, particles align in a preferential orientation; in many cases, the particles tend to align in the flow direction. Figure 1 shows the relevant microstructural parameters describing a single capsule. The relative deformation is quantified by the Taylor deformation parameter $D_{xy} = (L - l)/(L + l)$, where L and l are the major and minor semi-axes, respectively, of the deformed ellipsoidal particle in the xy plane. The orientation of the capsule relative to the flow (x) direction is given by θ. As detailed in Clausen & Aidun (2010), the microstructural parameters are calculated based on matching the moment of inertia for a model ellipsoid to the moment of inertia calculated during the simulation (Ramanujan & Pozrikidis 1998).

3. The simulation method

In order to gain insight into suspensions of deformable capsules, a hybrid simulation method has been developed that couples a LB fluid solver to a FE solid-body solver.

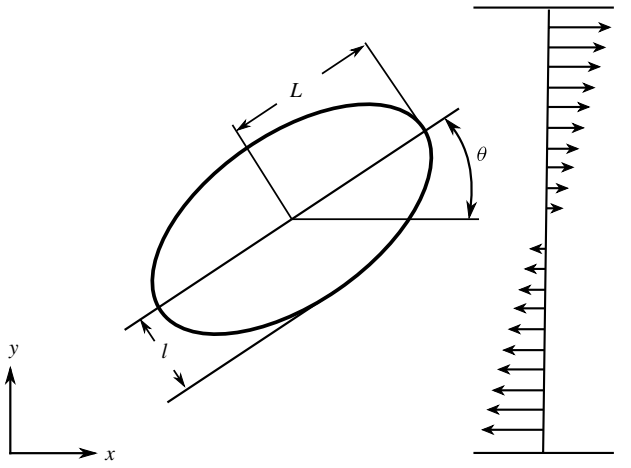

FIGURE 1. Description of single-body microstructure parameters for an initially spherical capsule that has deformed into an ellipsoidal shape.

This method, referred to as LB/FE, has been published previously (MacMeccan 2007; MacMeccan *et al.* 2009; Clausen & Aidun 2010) and validated for simulating capsule dynamics and dense suspension rheology. It is capable of performing simulations with up to 221 184 deformable spherical capsules on massively parallel architectures (Clausen *et al.* 2010). This section will provide a brief overview of both the LB and FE methods, as well as the coupling used in the hybrid LB/FE method.

3.1. *Lattice-Boltzmann method*

The fluid governing equations are approximated via the LB method, which was introduced over two decades ago as a method to smooth statistical fluctuations in lattice-gas automata (Frisch *et al.* 1987; McNamara & Zanetti 1988; Higuera & Jimenez 1989). The LB method can be shown to converge to the Navier–Stokes equations using a diffusive scaling (Junk & Yong 2003) or the more traditional two-scale Chapman–Enskog expansion (see for example Chen & Doolen 1998). The LB method has seen widespread application in areas as varied as particulate suspensions (Ladd 1994*a*,*b*; Aidun & Lu 1995; Aidun *et al.* 1998), multiphase flow (Nourgaliev *et al.* 2003), and turbulence (Vahala *et al.* 2009). The authors refer readers with interest in the LB method to the review articles by Chen & Doolen (1998) and Aidun & Clausen (2010).

The LB method is based on a discretization of the Boltzmann equation in velocity space, with microscopic velocities given by $\boldsymbol{e}_i$, where $i = 1 \ldots Q$. The LB method in this paper is three-dimensional and contains $Q = 19$ directions (referred to as D3Q19). A distribution of fluid particles, f_i, exists at discrete lattice nodes given by the position vector $\boldsymbol{r}$. The fluid particles undergo a streaming and collision process (Bhatnagar, Gross & Krook 1954) governed by the LB equation, shown as

$$f_i(\boldsymbol{r} + \boldsymbol{e}_i, t + 1) = f_i(\boldsymbol{r}, t) - \frac{1}{\tau}(f_i(\boldsymbol{r}, t) - f_i^{(eq)}(\boldsymbol{r}, t)) \tag{3.1}$$

where t is time, τ is the characteristic relaxation time that is related to the kinematic viscosity by $\nu = (2\tau - 1)/6$ and $f_i^{(eq)}$ is the equilibrium distribution function. The LB

Mach number is defined as $Ma = u/c_s$, where the LB pseudo-sound-speed is taken to be $c_s = \sqrt{1/3}$ throughout this paper with $\tau = 1$. The equilibrium distribution function is a function of the macroscopic fluid properties, such that

$$f_i^{(eq)} = w_i \rho [1 + 3(\boldsymbol{e}_i \cdot \boldsymbol{u}) + \tfrac{9}{2}(\boldsymbol{e}_i \cdot \boldsymbol{u})^2 - \tfrac{3}{2}u^2], \tag{3.2}$$

where w_i are lattice constants, ρ is the fluid density and $\boldsymbol{u}$ is the macroscopic fluid velocity. For the D3Q19 method, w_i are 1/3, 1/18 and 1/36 for the rest, non-diagonal and diagonal directions, respectively. The macroscopic fluid variables are related to moments in the equilibrium distribution function, shown as

$$\sum_{i=1}^{Q} f_i^{(eq)}(\boldsymbol{r}, t) = \rho, \quad \sum_{i=1}^{Q} f_i^{(eq)}(\boldsymbol{r}, t)\boldsymbol{e}_i = \rho \boldsymbol{u}, \quad \sum_{i=1}^{Q} f_i^{(eq)}(\boldsymbol{r}, t)\boldsymbol{e}_i\boldsymbol{e}_i = \frac{1}{3}\rho \boldsymbol{I} + \rho \boldsymbol{u}\boldsymbol{u}, \tag{3.3}$$

where $\boldsymbol{I}$ is the identity tensor. The LB method converges to the full Navier–Stokes equations in the long-time limit, thus the Stokes equations shown in § 2 are approximated by performing simulations at small Reynolds numbers. The effect of finite inertia is discussed in § 4.1.2.

3.2. *Finite-element method*

The elastic capsules are modelled using a linear-elastic FE model (MacMeccan *et al.* 2009). This model integrates the solid constitutive model across the finite but small width of the elastic membrane to recover standard elastic shell finite elements. The finite thickness does impart a resistance to membrane bending; however, the reduced bending ratio, $E_b = \kappa_b/a^2 E_y t_m$, is $O(10^{-5})$, thus bending effects are of negligible importance. In general, we do not see issues with membrane instability and buckling reported by other authors (Lac *et al.* 2004; Barthès-Biesel 2009), which may be due to the finite bending stiffness or the relative coarseness of the FE mesh. The time evolution of the FE nodal displacements, $\boldsymbol{x}$, and its derivatives is governed by the FE equation,

$$\boldsymbol{M}\ddot{\boldsymbol{x}} + \boldsymbol{C}\dot{\boldsymbol{x}} + \boldsymbol{K}\boldsymbol{x} = \boldsymbol{F}, \tag{3.4}$$

where $\boldsymbol{M}$ is the mass matrix, $\boldsymbol{C}$ is the damping matrix, $\boldsymbol{K}$ is the stiffness matrix and $\boldsymbol{F}$ is the applied force vector obtained from the fluid–solid coupling. As with the LB method, this FE formulation accounts for finite inertia, with the governing equation for the solid motion given in § 2 approximated by performing simulations at small Reynolds number. The FE matrix construction is detailed in MacMeccan *et al.* (2009). A body-fixed coordinate system tracks the average translation and angular displacement of the FE mesh, thus rendering all FE matrices invariant in the body-fixed frame. The two-coordinate method allows for an efficient integration of (3.4) using Newmark's method (MacMeccan *et al.* 2009). The level of mesh discretization is defined by l_{FEA}, which is the average FE edge length non-dimensionalized by the LB grid spacing.

3.3. *Fluid–solid coupling*

Coupling between the FE capsule and the LB fluid is accomplished through the bounce-back operation which is common in the LB literature (e.g. Ladd 1994*a*,*b*; Aidun *et al.* 1998; Aidun & Clausen 2010). The bounce-back operation is predicated on boundary links (BLs) that intersect the capsule surface and connect LB nodes along the discrete velocity vectors, $\boldsymbol{e}_i$. The bounce-back operation adjusts the momentum of fluid distributions residing at the LB nodes at either end of the BL to impose the

no-slip hydrodynamic boundary condition (for details, see Aidun & Clausen 2010), and for arbitrarily shaped boundaries, the bounce-back method is first-order accurate in space (Ginzbourg & Adler 1994). For fluid-filled capsules, the momentum of both internal and external LB nodes are adjusted, and an equal and opposite force is interpolated to the FE membrane nodes, as was detailed in MacMeccan *et al.* (2009). Numerical integration of (2.5) requires the external traction vectors acting on the capsule's surface, thus only the momentum imparted by bouncing the external fluid distribution is included in the stresslet calculation. This creates a Galilean error in the LB method (Clausen & Aidun 2009; Lorenz, Caiazzo & Hoekstra 2009), which is corrected using the internal boundary node method discussed in Clausen & Aidun (2009). A new method has been recently introduced that is based on a smooth interpolation of forces and not on a linkwise bounce-back procedure. This technique, the external boundary force method, shows promise in improving the stability of the fluid–solid coupling (Wu & Aidun 2009, 2010). The results show reduced oscillations in the force and torque acting on the particle as it traverses the underlying fluid mesh, which results in a smoother particle trajectory than the bounce-back method (Wu & Aidun 2009).

Accurately recovering the isotropic pressure associated with the particle pressure requires awareness of several subtleties in the LB method, as detailed in Clausen & Aidun (2010). First, the LB method has a mean pressure associated with the LB equation of state, $P_f = \langle\rho\rangle_f c_s^2$, where this pressure has been neglected by subtracting it from external traction forces used in the stresslet calculation (2.5). Note that for strictly incompressible suspensions, the mean pressure is constant and not a function of the flow field, since the mean density is constant within the fluid. However, the LB method is pseudo-compressible, and small changes in density result in large changes in pressure. Thus, as an initially spherical particle deforms, the increase in internal pressure is equivalent to an increase in the internal density. Owing to conservation of mass, the external fluid's density decreases slightly, which can alter the mean static pressure in the fluid and bias the particle pressure calculation if this drift is not accounted for in the stresslet calculation.

At small times, the LB method approximates the incompressible nature of the suspended capsules; however, at longer times, the high-density internal fluid 'leaks' through the capsule membrane as high-density LB nodes are uncovered when the FE mesh traverses the underlying LB grid. Consequently, particle volume decreases gradually in proportion to the leaked mass, and particle incompressibility is not maintained. Instead of relying on the LB method, particle incompressibility is enforced by augmenting the internal bounce-back operation to create an artificial internal pressure that is a stiff function of the relative change in particle volume. The resultant force acting on the membrane from the LB bounce-back operation becomes

$$\boldsymbol{F}^{(b,\Delta P)} = 2\boldsymbol{e}_i[f_i(\boldsymbol{r}, t^+) + f_i^{\Delta P} - 3\rho\omega_i \boldsymbol{u}_b \cdot \boldsymbol{e}_i], \tag{3.5}$$

where $\boldsymbol{u}_b$ is the boundary velocity, and t^+ denotes a time post-collision but pre-propagation. The adjustment takes the form

$$f_i^{\Delta P} = w_i \rho_0 \left(\frac{V_0}{V_p} - 1 \right), \tag{3.6}$$

where ρ_0 is the initial density inside the particle, V_0 is the initial particle volume and V_p is the current particle volume (Clausen & Aidun 2010). In typical simulations, the percentage change in the volume of the capsules is less than 0.02 %. To account for

the mass leakage and consequent alteration to the static portion of the LB pressure, the average density of the internal and external fluids are altered to be equal to the mean density. This is accomplished through a brute-force adjustment to all lattice distributions, $f_i^{\Delta\rho} = w_i \Delta\rho$, where $\Delta\rho$ is the change in density needed to restore the appropriate mean value (Clausen & Aidun 2010).

The original subgrid model formulated in MacMeccan *et al.* (2009) has several shortcomings that preclude the accurate resolution of lubrication hydrodynamics when two particles are near contact. As formulated in MacMeccan *et al.* (2009), the contact function and constants keep particles separated beyond the regime where subgrid lubrication modelling becomes important, i.e. the contact function is too soft. Therefore, lubrication modelling is not applied except in cases where the particles are forced into contact, e.g. the test case presented in MacMeccan *et al.* (2009). Unfortunately, stiffening the contact function enough for the subgrid lubrication modelling to become relevant results in unstable particle dynamics. These instabilities are driven by the singular nature of lubrication hydrodynamics and uncertainties in the particle border due to the discrete nature of linkwise separation distance calculation. These stability issues are mentioned in MacMeccan *et al.* (2009) and discussed in detail in Clausen (2010). Consequently, the results presented in this paper do not use subgrid lubrication modelling, but they do retain the contact function originally presented in MacMeccan *et al.* (2009). The result is an accurate description of hydrodynamics down to 0.5 lattice spacing (5 % of a particle radius assuming $a = 10$). Below this distance, separation is enforced through the exponential contact function. The implications associated with this limitation are discussed in the context of suspension rheology in § 4.2.

4. Dense capsule suspensions

Previous research using the LB/FE method has studied the dilute-limit impact of capsule deformation on suspension rheology (Clausen & Aidun 2010). While the dilute-limit effect of a spherical particle is constrained to the shear components of the suspension stress (Σ_{12} and Σ_{21}), a capsule deforms in linear shear into an ellipsoidal shape with a preferential orientation; therefore, non-Newtonian effects are seen including normal stress differences and a non-zero particle pressure (Clausen & Aidun 2010). This research will explore the influence of capsule deformation in more concentrated suspensions. Similarly to Stokesian dynamics, simulations are performed in a periodic domain in which a linear shear field is imposed to assess the impact of capsule deformation on the rheology and microstructure of these flows. In this setup, the flow and vorticity directions are typical periodic boundary conditions, and the shear direction undergoes a periodic straining motion. Numerically, this is implemented in the context of the LB method through a Lees–Edwards boundary condition (Wagner & Pagonabarraga 2002), in which fluid and particles crossing the domain boundary in the shear direction undergo an adjustment in velocity and location to account for the shearing motion (see MacMeccan *et al.* 2009; Aidun & Clausen 2010, for details). The LB Mach number is less than 0.03 in all cases; therefore, compressibility errors are expected to be negligible. A snapshot from a typical simulation can be seen in figure 2, in which 285 deformable particles with $Ca_G = 0.02$ are shown in an periodic shear domain. Initial particle locations are determined by a random seeding and growth process (MacMeccan 2007). In this process, particles are seeded at a fraction of their final size in random locations. Then, the particle size is

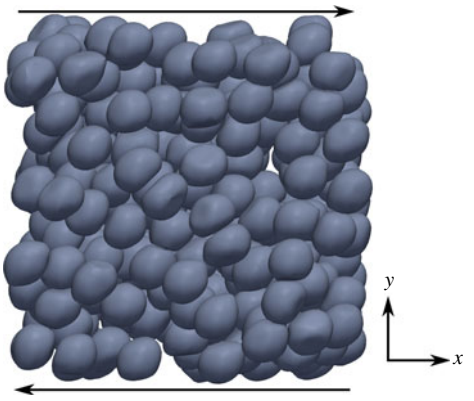

FIGURE 2. Snapshot of typical simulation of $N = 285$ initially spherical capsules with $Ca_G = 0.02$.

gradually increased as the particles are allowed to interact hydrodynamically. Particles are not allowed to deform during the seeding and growing process.

4.1. *Sensitivity to parameters*

The LB/FE simulation technique has been validated using a variety of model problems (MacMeccan *et al.* 2009) and a detailed study into dilute-limit tank-treading capsule dynamics (Clausen & Aidun 2010); however, it is helpful to revisit the sensitivity of the rheology and microstructure in dense capsule suspensions to several key parameters including the number of particles, particle inertia and averaging time.

4.1.1. *Number of particles and simulation repeatability*

The rheology and microstructure measurements are average quantities, and as such, a large enough number of particles is required to achieve converged statistics. In dense suspensions, these parameters can show large fluctuations, and achieving reliable estimates of these quantities requires a significant number of particles simulated for large times (>30 strain units, $\dot{\gamma}t$). Test simulations are performed in periodic shear (Lees–Edwards boundary condition) with a moderate level of deformation ($Ca_G = 0.02$) at 40 % volume fraction, although some small variance in volume fraction exists due to the integer nature of the number of particles and the domain size. In all cases, the undeformed particle radius is 10 lattice spacings, the discretization is such that $l_{FEA} = 2.0$ and $Re_p = 0.067$. Simulations are performed at $N = 25$, 50, 97 and 285 deformable capsules.

Converged values for the rheological and microstructural parameters of interest are calculated through a combined volume and time average. First, the instantaneous average suspension stress is calculated according to (2.4) and (2.5). The average microstructure parameters for the capsules are calculated individually, then averaged over N capsules. Figure 3(*a–c*) show the transient behaviour of the deformation index, relative viscosity and first normal stress difference for several N as thin lines. After the initial transient has subsided (≈10 strain units), a time-average is started from that point forward. The time averages are shown in figure 3(*a–c*) as the thick lines beginning at 10 strain units. The Taylor deformation parameter and relative suspension viscosity are generally insensitive to changes in N, although the low-particle-count cases do display larger fluctuations, as seen in the instantaneous values. The first normal stress differences show especially large fluctuations in the instantaneous

N	25	50	97	285
Domain	64^3	80^3	100^3	144^3
ϕ	39.20	40.14	39.87	39.23
D_{xy}	0.1186	0.1197	0.1200	0.1173 ± 0.0004
θ/π	0.2161	0.2176	0.2165	0.2191 ± 0.0004
μ_r	3.370	3.444	3.426	3.342 ± 0.0032
$N_1/\mu\dot{\gamma}$	0.9157	0.9060	0.9448	0.8322 ± 0.0108
$N_2/\mu\dot{\gamma}$	−0.3505	−0.3413	−0.3949	-0.3771 ± 0.0070
$\Pi_p/\mu\dot{\gamma}$	0.2838	0.2939	0.2795	0.2711 ± 0.0120

TABLE 1. Converged microstructure and rheology parameters for $Ca_G = 0.02$ simulations as a function of the number of particles, N. Range at $N = 285$ represents two standard deviations calculated by four separate time averages.

particle-averaged results, with the $N = 25$ and 50 cases showing poor time-averaged convergence. Qualitatively, cases with less deformation show larger fluctuations in the instantaneous parameters, particularly the normal stress differences (not shown). The converged values for all parameters of interest are listed in table 1 with values representing a time average from 10 to 40 strain units. For the case of $N = 285$, a simulation of 130 strain units is performed to allow averaging over independent 30 strain unit periods (10–40, 40–70, etc.). After 30 strain units, the particle locations are no longer correlated to their starting positions; therefore, the results from each 30 strain unit window are taken as samples of differing initial conditions. The value ranges found in table 1 for $N = 285$ represent the mean and a range of two standard deviations presented for the four sample windows; therefore, good repeatability is seen. The expected uncertainty would be much larger for the lower N cases, and a rigorous statistical test determining if N is significant is not possible without long simulations at all N.

4.1.2. *Reynolds number and particle discretization*

The primary interest of this study is in the limit of low-Reynolds-number (Stokes) flows; however, the LB method recovers inertial behaviour, thus a small amount of inertia will be present. Furthermore, reducing Re_p requires decreasing the shear rate, which increases the number of time steps necessary to reach a given non-dimensional time. Increasing the fluid viscosity is possible, but without higher-order bounce-back schemes (d'Humières *et al.* 2002; Aidun & Clausen 2010), higher viscosities result in increased error in the bounce-back boundary condition (Noble *et al.* 1995; Ladd & Verberg 2001; Ding & Aidun 2003). To demonstrate the effect of inertia, the 40 % volume fraction case with 285 particles from the previous section is simulated at $Re_p = 0.0067$, 0.067 and 0.67, and the transient and time-averaged behaviour of D_{xy}, μ_r and N_1 is shown in figure 4(*a–c*). All simulations use $l_{FEA} = 2.0$ except where noted. The high-Re_p case shows a noticeable shift in the rheology and microstructure results, although the deviation is relatively small ($\approx$10 % for the first normal stress difference) when compared with the baseline case ($Re_p = 0.067$). The small-magnitude Re_p simulation exceeds the current computational capabilities; however, the short-time behaviour shows excellent agreement with the baseline $Re_p = 0.067$ case, as seen in the zoomed insets in figure 4(*a–c*). In contrast, the error in the high-Re_p case is evident even in the initial transient. Taken together, these two observations suggest that the Reynolds number effects are negligible at $Re_p = 0.067$. The difference between the fine discretization ($l_{FEA} = 1.5$) case and the baseline ($l_{FEA} = 2.0$) is minimal.

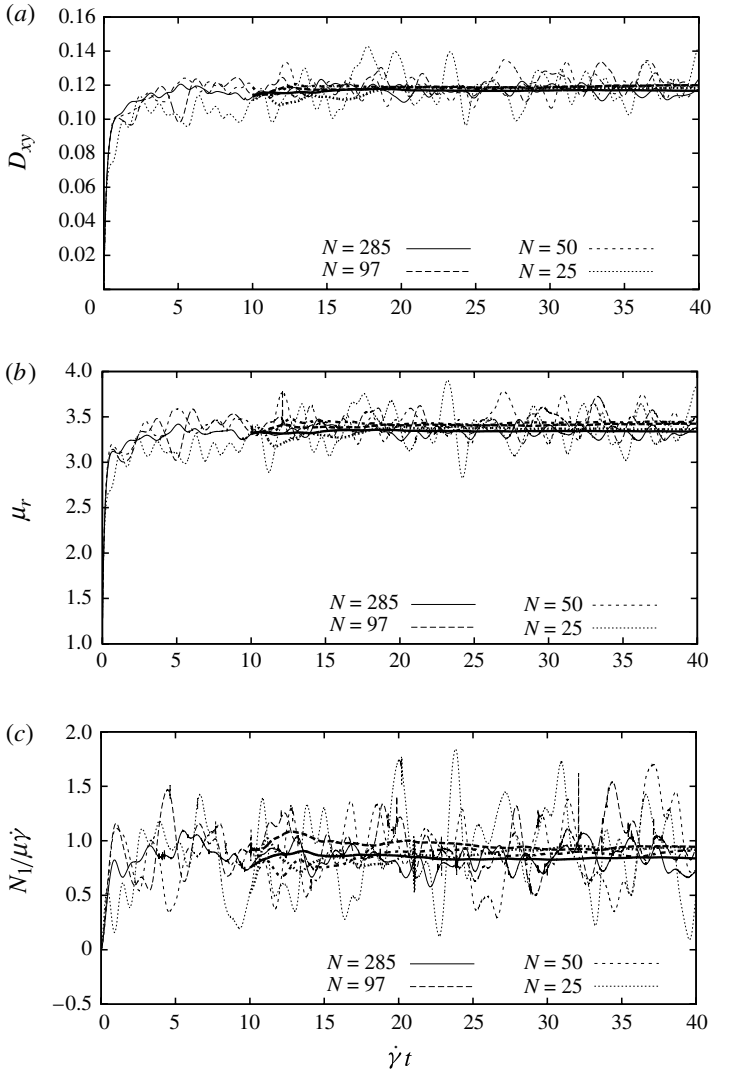

FIGURE 3. Transient behaviour for simulations of a varying number of particles, N. Results show (a) the deformation index, (b) the relative suspension viscosity and (c) the first normal stress difference. Thin lines show transient behaviours, while thick lines show time-averaged values starting at $\dot{\gamma}t = 10$.

Other microstructure and rheology results not shown in figure 4(a–c) show similar behaviour. Accordingly, all subsequent simulations will be performed with $\approx$200 particles, $l_{FEA} = 2.0$ and $Re_p = 0.067$.

We must stress that although inertial effects are negligible with regards to the calculation of the particle stresslet according to (2.5), there may still be significant inertial effects. Equation (2.5) has neglected any inertial terms explicitly; therefore, the only remaining inertial effects enter into the calculation through alteration to the suspension microstructure. These alterations appear to be negligible at $Re_p = 0.067$ according to figure 4, thus our calculations approximate the Stokes flow solution. Other researchers have reported inertial effects that may not be negligible at

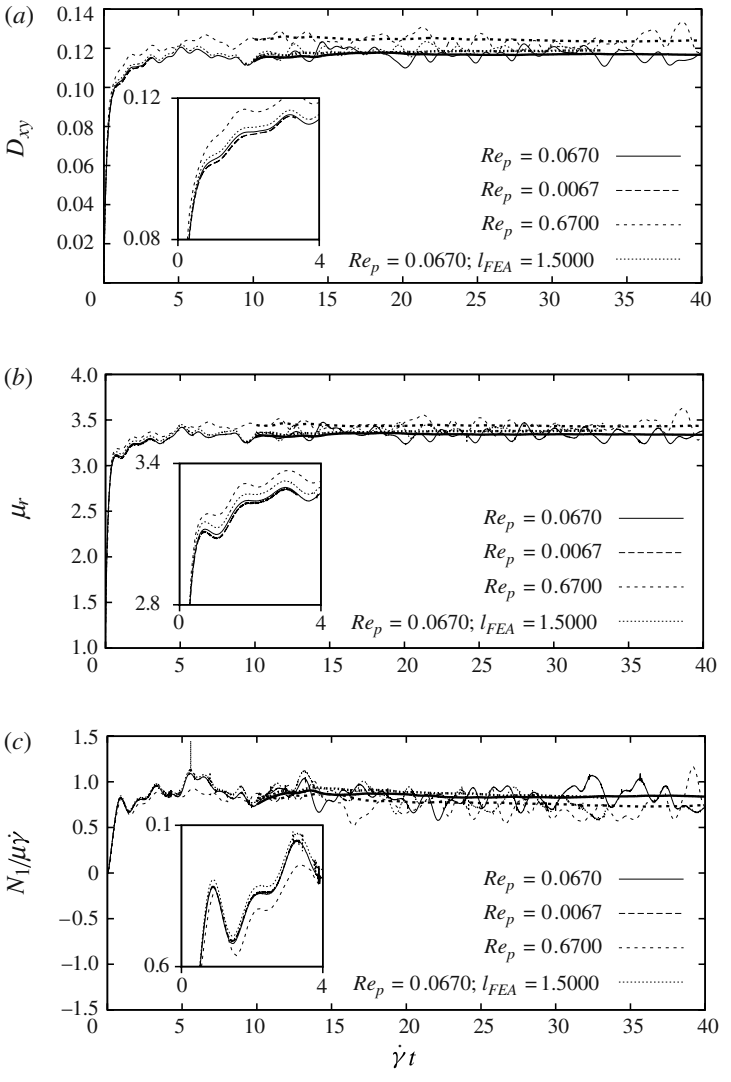

FIGURE 4. Transient behaviour of microstructure and rheology results for a suspension of $N = 285$ capsules with $Ca_G = 0.02$ as a function of Re_p. Results show (*a*) the deformation index, (*b*) the relative suspension viscosity and (*c*) the first normal stress difference, with short-time transient behaviour shown in inset. Thin lines show transient behaviours, while thick lines show time-averaged values starting at $\dot{\gamma}t = 10$.

$Re_p \sim 0.05$, although in all cases they properly include the inertial terms in the stresslet calculation (Lin, Peery & Schowalter 1970; Kulkarni & Morris 2008).

4.2. *Comparison with rigid results*

Although results for deformable particle suspensions are somewhat lacking, a large body of research exists for suspensions of rigid spheres in the limit of negligible inertia (see Stickel & Powell 2005, for review). Accordingly, simulations are performed using the LB/FE method with no particle deformation ($Ca_G = 0$), no Brownian motion ($Pe \to \infty$) and in the limit of negligible inertia. This region

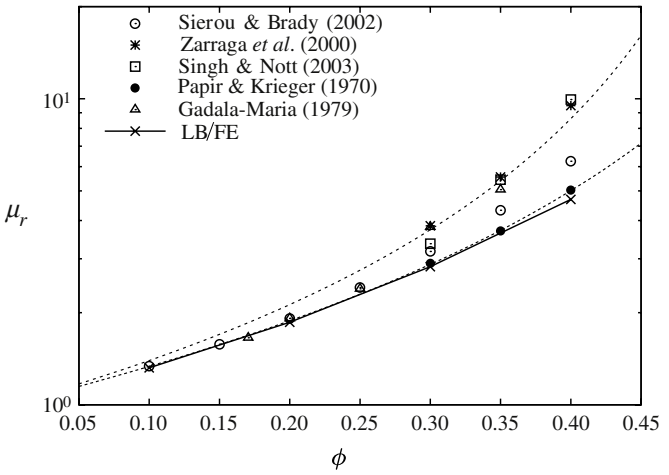

FIGURE 5. Relative viscosity as a function of the volume fraction for rigid sphere suspensions. Empirical fits include the Krieger–Dougherty relation (- - -) for the data of Papir & Krieger (1970) and the Eilers fit (– · –) for the data of Zarraga *et al.* (2000).

corresponds to the so-called high-shear viscosity regime, and is ideally treated as Newtonian (Stickel & Powell 2005). Theoretically, the suspension viscosity is strictly a function of the volume fraction, and many attempts have been made to fit empirical curves to rheological data in this regime. Common fits include the Krieger–Dougherty relation (Krieger & Dougherty 1959),

$$\mu_r = \left(1 - \frac{\phi}{\phi_m}\right)^{-[\mu]\phi_m}, \tag{4.1}$$

and the fit of Eilers (1941) (taken from Zarraga *et al.* 2000),

$$\mu_r = \left(1 + \frac{1.5\phi}{(1 - \phi/\phi_m)}\right)^2, \tag{4.2}$$

where ϕ_m is the maximum packing fraction and $[\mu]$ is the intrinsic viscosity. In practice, suspensions are less ideal than these relations suppose, and ϕ_m and $[\mu]$ are used as fitting parameters. For example, Papir & Krieger (1970) suggest using $\phi_m = 0.68$ and $[\mu] = 2.67$ in (4.1) to accurately fit the high-shear viscosity of polystyrene spheres with $a = 75$–215 nm in benzyl alcohol or metacresol, with both empirical fit (4.1) and data shown in figure 5. These viscosities are significantly lower than those reported by Zarraga *et al.* (2000), who use $\phi_m = 0.58$ in (4.2) to fit the rheological data from spheres ranging from 43.0 to 73.6 μm in size. In addition, many suspensions are known to be shear thinning at regions well past the transition from the low- to high-shear limits (Zarraga *et al.* 2000; Stickel & Powell 2005), an effect which is not captured in the above empirical fits and currently lacks explanation. Experimental data and fit from Zarraga *et al.* (2000) are shown in figure 5, along with experimental data from Gadala-Maria (1979) (data taken from Sierou & Brady 2002) and Singh & Nott (2003).

These deviations in rheology can be explained by differences in interparticle forces. Mewis *et al.* (1989) studied the rheology of suspensions with a variety of particle sizes, and found that when sterically stabilized, smaller particles were effectively softer

due to the relatively (in terms of the particle radius) longer-ranged interparticle forces. This observation is corroborated by SD simulations, also shown in figure 5, in which larger interparticle forces reduced the suspension viscosity (Sierou & Brady 2002). Since lubrication forces are dissipative in nature, the decreased suspension viscosity is a direct result of the larger interparticle gaps, and thus smaller lubrication forces, that are seen in the presence of larger repulsive interparticle forces.

The relative viscosity calculated from the LB/FE results for rigid suspensions in simple shear is also shown in figure 5. Excellent agreement between experimental and numerical results are seen at lower volume fractions, with some divergence seen at higher concentrations. The LB/FE results are among the lowest in viscosity; however, the results are within the range measured experimentally. Good agreement is seen between the results of Papir & Krieger (1970) and the LB/FE simulations. The LB/FE simulation results and Papir & Krieger (1970) experimental results share the attribute that the suspensions tested contain the relatively largest-ranged interparticle repulsive forces. In addition, the LB/FE method fails to resolve lubrication hydrodynamics in the near-contact limit, thus reducing the measured viscosity.

Experimentally measuring the normal stresses in suspensions of rigid spherical particles is much more challenging than measuring the viscosity. Gadala-Maria (1979) first observed the presence of normal stresses in these suspensions; however, his results were subject to large errors. More recent results by Zarraga *et al.* (2000) used a variety of techniques that included using the resuspension data of Acrivos, Mauri & Fan (1993), parallel-plate and cone-and-plate viscometers, and surface profilometry to accurately resolve the separate normal stress components, as shown in figure 6(*a–c*). Zarraga *et al.* (2000) proposed the following empirical fits to their data:

$$\left.\begin{aligned} \frac{\Sigma_{11}}{\mu_r \mu \dot{\gamma}} &= -2.50\phi^3 \mathrm{e}^{2.34\phi} \\ \frac{\Sigma_{22}}{\mu_r \mu \dot{\gamma}} &= -2.17\phi^3 \mathrm{e}^{2.34\phi} \\ \frac{\Sigma_{33}}{\mu_r \mu \dot{\gamma}} &= -\phi^3 \mathrm{e}^{2.34\phi}. \end{aligned}\right\} \tag{4.3}$$

Also shown are the results of Singh & Nott (2003), in which the normal stress differences were measured using a sinusoidal varying shear rate in a combination of parallel-plate and Couette viscometers. The isotropic portion of the particle stress shown in figure 6(*c*) is calculated using the fitted data of Zarraga *et al.* (2000) and is measured directly by Deboeuf *et al.* (2009). In Deboeuf *et al.* (2009), the particle pressure is measured by attaching a screened manometer tube to the side of a continuously sheared Couette viscometer. The increase in particle pressure creates an effect analogous to that of an osmotic pressure, i.e. the partial pressure of the fluid phase decreases. Thus, the shearing motion of the suspension creates a drop in the fluid pressure as measured in the manometer. The scatter in results correspond to measurements with various sized particles.

The LB/FE results agree well with the experimental results of Singh & Nott (2003) for N_1 at high volume fraction, as seen in figure 6(*a*). At higher concentrations, a qualitative agreement is seen with the empirical fit of Zarraga and the SD results of Sierou & Brady (2001); however, at lower volume fractions, some deviation in the LB/FE results is seen. In general, the empirical fit of Zarraga underpredicts N_1 relative to other experimental and numerical methods. The deviation between the LB/FE results and the other results at low volume fraction could be the

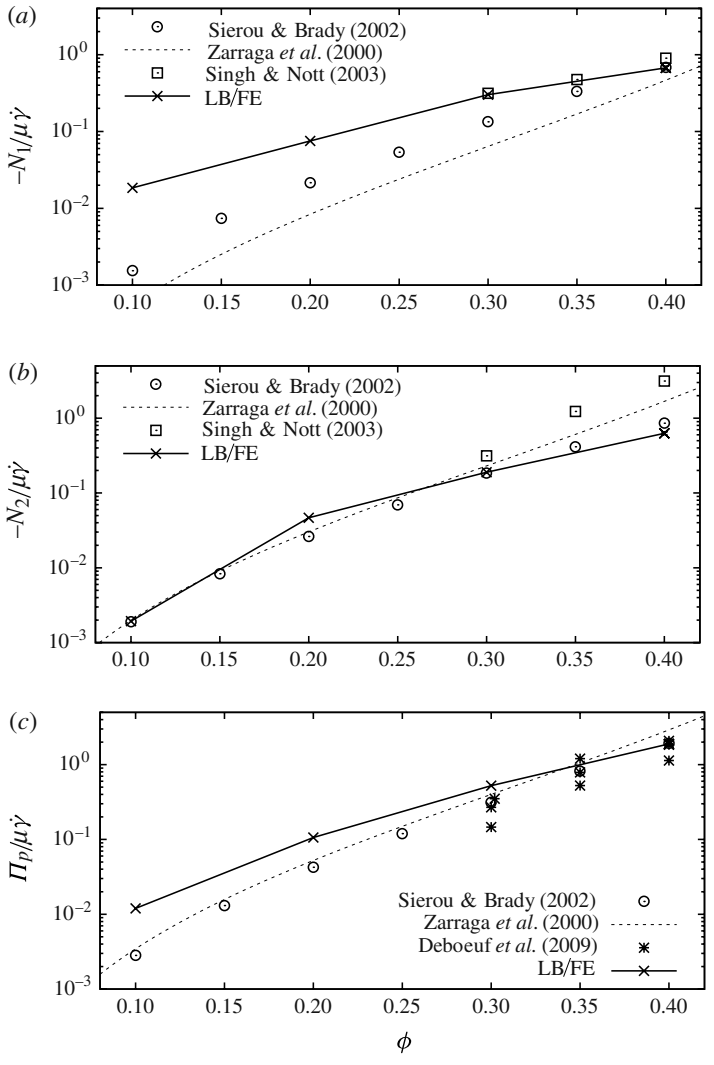

FIGURE 6. Normal stress results for suspensions of rigid spherical particles in periodic shear as a function of volume fraction. Results show (*a*) the first normal stress difference, (*b*) the second normal stress difference and (*c*) the particle pressure.

result of numerical errors because the magnitude of N_1 is exceedingly small at these concentrations. The four methods show much better agreement with respect to N_2, as seen in figure 6(*b*), where the LB/FE and SD methods tend to predict lower magnitudes than the experimental results. Experimental studies tend to find $N_2 < N_1 < 0$, while the numerical results of the LB/FE method and SD put the first and second normal stresses at roughly the same magnitude. The interparticle force has been implicated in this discrepancy (Singh & Nott 2003), although this theory is inconclusive. Particle pressure results are not available from Singh & Nott (2003); however, decent agreement is seen between the empirical fit (Zarraga *et al.* 2000), the results of Deboeuf *et al.* (2009), SD simulations (Sierou & Brady 2002) and the LB/FE method, as seen in figure 6(*c*).

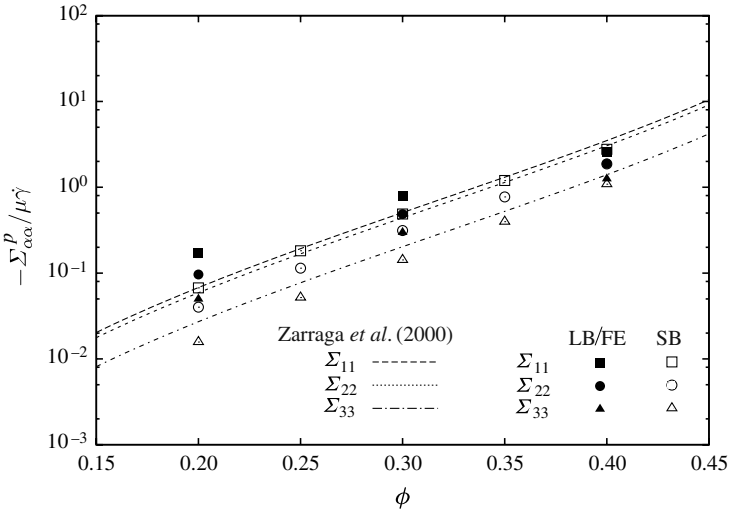

FIGURE 7. Individual components of the normal stresses as a function of volume fraction. LB/FE results are shown as solid symbols, Sierou & Brady (2002) (SB) results are shown as outlined symbols and the proposed empirical fits of Zarraga *et al.* (2000) are shown as dashed lines.

The individual normal stress components are shown in figure 7. Qualitatively, experimental, SD and LB/FE results show increasingly negative normal stress components, with $\Sigma^p_{11} < \Sigma^p_{22} < \Sigma^p_{33} < 0$; however, quantitative differences exist. The empirical fit of Zarraga *et al.* (2000) shows a smaller difference between Σ^p_{11} and Σ^p_{22}, while both the LB/FE and SD results (Sierou & Brady 2002) show larger differences, as seen in figure 7. This smaller difference in $\Sigma^p_{11} - \Sigma^p_{22}$ was also seen as a lower magnitude N_1 in figure 6(*a*). While the SD results follow the fit of Zarraga *et al.* (2000) reasonably well, the LB/FE results diverge at lower volume fractions where the magnitude of the normal stresses is quite small. Nevertheless, the LB/FE method is a useful tool for probing suspension rheology.

4.3. *Deformable suspensions*

Now that the rheological behaviour and accuracy of the LB/FE method has been demonstrated in the rigid limit, a detailed study characterizing the effect of particle deformation is performed. In dense suspensions, the elasticity parameter is more accurately scaled by defining an effective capillary number,

$$Ca_{G,eff} = \frac{\mu_r \mu \dot{\gamma} a}{G_M}, \tag{4.4}$$

in which the viscous stresses are scaled by the effective suspension viscosity ($\mu_r \mu$).

Figure 8 shows the shear-thinning behaviour of capsule suspensions as the deformation of the solid phase is increased. At high concentrations, the shear thinning is much more pronounced. For the $\phi = 0.4$ case, the relative viscosity decreases from 4.7 to 3.0 over the range of $Ca_{G,eff}$ simulated. In contrast to dilute capsule suspensions (Ramanujan & Pozrikidis 1998; Clausen & Aidun 2010), the decrease in viscosity is most prominent in the near-rigid limit. This behaviour implies that the initial reduction in viscosity is driven by changes in the particle interactions, hence altering the configurational microstructure, and not by the single-body change in particle shape.

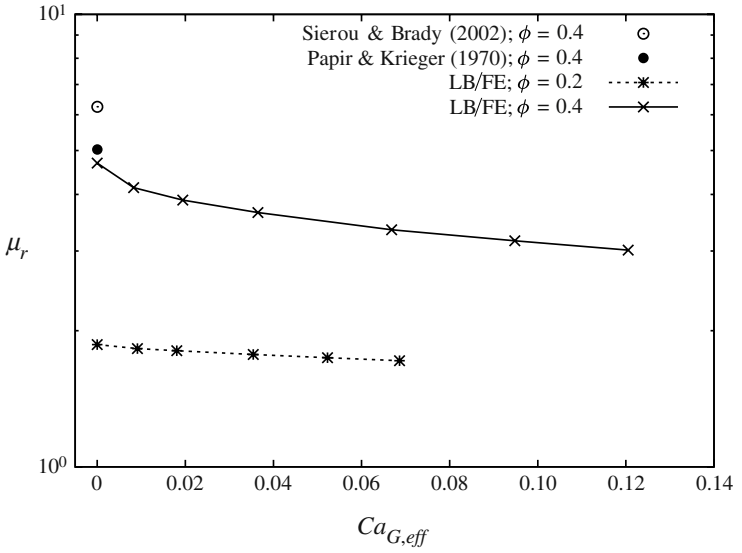

FIGURE 8. Relative viscosity of capsule suspension as a function of the elasticity parameter $Ca_{G,eff}$. Volume fractions of 20 % and 40 % are shown.

Also, capsules can attain higher packing fractions due to deformation, which will affect the suspension viscosity at high concentrations. The suspension microstructure is examined in more detail in § 4.4.

Figure 9 shows the behaviour of the normal stresses as deformation is increased. The first normal stress difference, shown in figure 9(*a*), undergoes a change in sign. For rigid suspensions, a negative first normal stress difference is observed owing to anisotropy in the particle configuration, which is also seen for the rigid and near-rigid LB/FE simulation cases. As deformation is increased, the preferential orientation of individual capsules in the flow direction (Clausen & Aidun 2010) creates an overall positive Σ_{11} and negative Σ_{22}, i.e. positive N_1. Thus, the configurational microstructure and single-body microstructure introduce competing influences on the first normal stress difference. At $\phi = 0.2$, similar behaviour is seen; however, the magnitudes are much smaller. Both 20 % and 40 % concentrations appear to reach zero N_1 at similar $Ca_{G,eff}$, but it is not known whether this trend will continue for other concentrations. The second normal stress difference, shown in figure 9(*b*), remains negative with a slight decrease in magnitude due to capsule deformation. Perhaps most surprising is the particle pressure, shown in figure 9(*c*), which decreases rapidly with the onset of deformation. Some of this decrease is attributable to the negative pressure generated by an isolated capsule (Clausen & Aidun 2010); however, alterations in interparticle interactions and the configurational microstructure could also play a role.

Existing literature for the rheology of dense suspensions of deformable particles is scarce; however, some progress has been made for droplet suspensions. For example, Loewenberg & Hinch (1996) simulated as many as 12 deformable droplets using a boundary integral formulation, and qualitatively, the droplet dynamics are similar to elastic capsules. The initially spherical droplets deform into ellipsoids and align with the flow direction; a positive N_1 and negative N_2 are generated. Rheological measurements show qualitative differences, however, and in the limit as $Ca \to 0$, the rheology does not converge to those of rigid spheres. The capillary number is defined

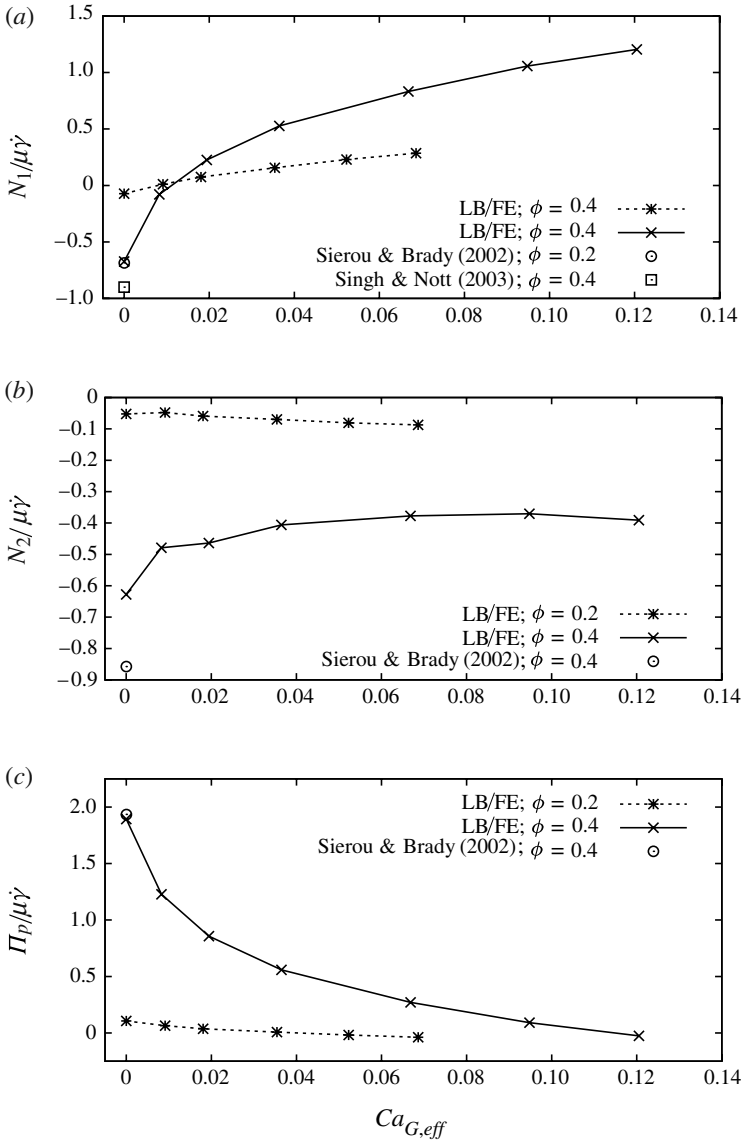

FIGURE 9. Normal stresses in capsule suspensions as a function of the elasticity parameter $Ca_{G,eff}$. Volume fractions of 20 % and 40 % are shown for (*a*) the first normal stress difference, (*b*) the second normal stress difference and (*c*) the particle pressure.

for droplets as $Ca = \mu\dot{\gamma}a/\gamma_{it}$, where γ_{it} is the interfacial tension. Instead, Loewenberg & Hinch (1996) reports zero normal stress differences. As deformation increases, rheology measurements do not appear to converge to a limiting value, but instead diverge, with N_1 rapidly increasing at $Ca \sim 0.4$. Particle pressure is not reported.

The boundary integral results of Zinchenko & Davis (2002) are in better qualitative agreement with the LB/FE results. In these simulations, up to 200 deformable droplets are simulated in periodic shear. Again, dynamics are similar, and positive N_1 and negative N_2 are seen. More importantly, rheology measurements appear to be converging as deformation increases, in contrast to the divergent behaviour

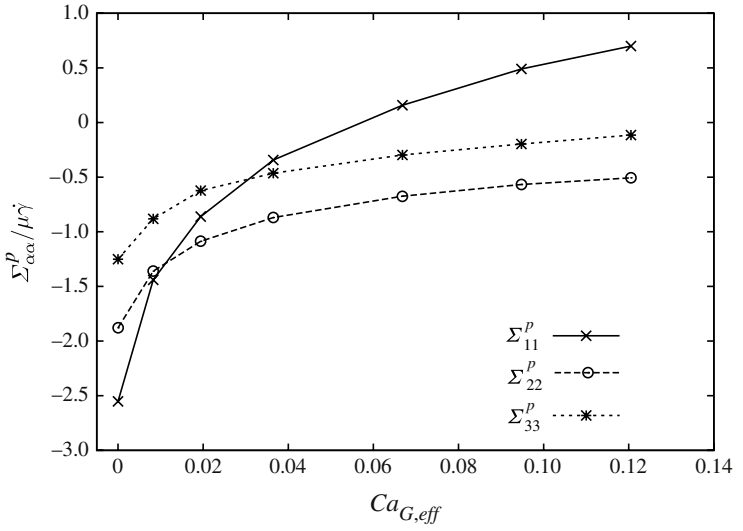

FIGURE 10. Individual normal stress components of the particle-phase stress tensor for capsule suspensions at 40 % concentration.

of Loewenberg & Hinch (1996). Simulation results are constrained to $Ca > 0.05$; therefore, it is difficult to make comparisons to rheology of rigid particle suspensions. Here N_1 is positive for all simulation results, although it appears that a negative value will be obtained prior to $Ca = 0.0$. Again, particle pressure results are not reported.

The individual components of the particle-phase stress tensor are reported as a function of the effective capillary number in figure 10 for the $\phi = 0.4$ concentration case. An overall shift towards tensile stresses is seen although Σ^p remains compressive for the shear-gradient and vorticity directions. In the flow direction, the tensile stresses are due to the elongation of the individual capsules as they align towards the flow direction.

4.4. *Capsule microstructure*

Quantifying the changes in suspension microstructure is critical to providing physical insight into the observed changes in suspension rheology caused by particle deformation. The dilute-limit microstructure for capsules has been studied using the LB/FE method for tank-treading capsules in Clausen & Aidun (2010). The average single-body microstructure is quantified in dense suspensions using the Taylor deformation parameter (D_{xy}) and the capsule orientation (θ), as defined in § 2. In addition, the configurational microstructure, as quantified by the pair-distribution function $g(\boldsymbol{r})$, is calculated.

Figure 11(*a*,*b*) show the average values of D_{xy} and θ as a function of the effective capillary number, $Ca_{G,eff}$, for a variety of concentrations. Average values were calculated by calculating D_{xy} and θ on a particle-by-particle basis, then taking a number average over all times that the rheology averages were calculated. If we assume that the average capsule deformation is a function of the average shear stress in a suspension, then the microstructure parameters D_{xy} and θ will be only weak functions of the volume fraction. The deformation parameter, shown in figure 11(*a*), largely behaves in this manner, especially as $Ca_G \to 0$; however, the orientation angle, θ, shows a shift towards the extensional axis at higher volume fractions. One

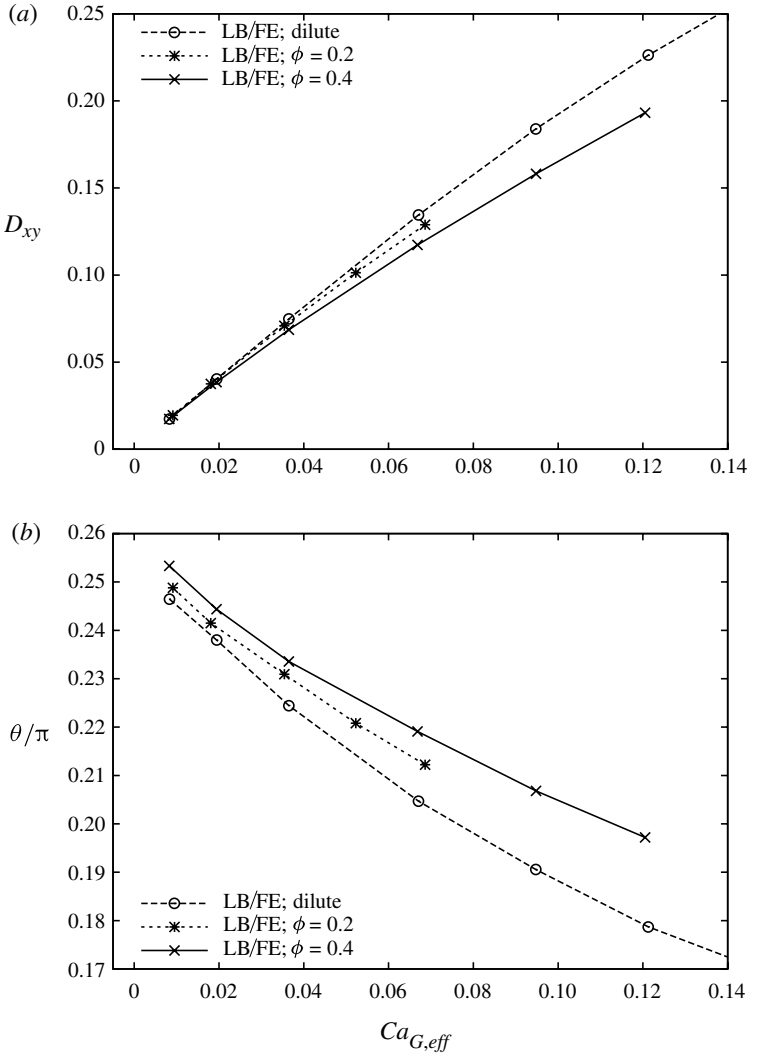

FIGURE 11. Single-body microstructure in capsule suspensions as a function of $Ca_{G,eff}$ showing the (*a*) Taylor deformation parameter and (*b*) orientation of the capsule with the flow (x) direction.

possible explanation for this shift could be the increased asymmetry found in the pair-distribution function at higher concentrations (Sierou & Brady 2002), which acts to apply a torque on the particle driving the orientation away from the flow direction.

Since the single-body microstructure is not affected heavily by altering the concentration, the large deviations in suspension rheology must be attributed to changes in the particle–particle interactions and the associated changes to the configurational microstructure. This effect can most easily be demonstrated by plotting the average single-particle stresslet value for various concentrations, as shown in figure 12. The average stresslet has been defined as $\langle \boldsymbol{S} \rangle = 1/N \sum \boldsymbol{S}$, and the results have been normalized by the dilute-limit contribution of an isolated sphere, $S^s_{12} = 10/3\pi a^3 \mu \dot{\gamma}$. The average stresslet corresponds to the mean influence of a single

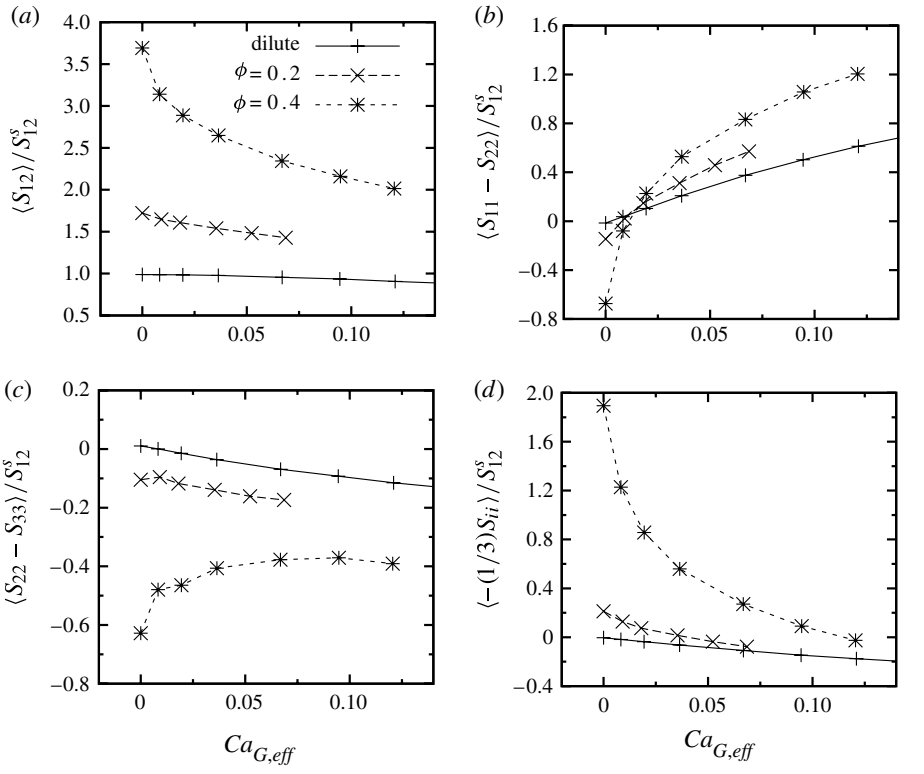

FIGURE 12. Average stresslet values illustrating the influence of a single particle on rheology for (*a*) the viscosity, (*b*) the first normal stress, (*c*) the second normal stress and (*d*) the isotropic contribution. Stresslet values have been normalized by the dilute-limit contribution of an isolated sphere, S^s_{12}. The large deviation in particle stresslet values for various concentrations highlight the importance of interparticle interactions. The legend in (*a*) is valid throughout. Dilute results taken from Clausen & Aidun (2010).

particle to the suspension rheology. Note that while the single-body microstructure is similar for a given effective capillary number according to figure 11, the average stresslet values are markedly different. The deviation in the average stresslet from the dilute case illustrates the importance of many particle interactions, which is not unexpected considering the influence of concentration in rigid suspensions. The notably different behaviour of the average stresslet as deformation is increased highlights the importance of deformation in altering particle interactions: an entirely dilute-limit influence of particle deformation on rheology would result in the similar behaviour of the average stresslet values as a function of $Ca_{G,eff}$.

The pair distribution function is calculated for the LB/FE simulations using a standard binning procedure (Morris & Katyal 2002), and asymmetry in the pair-distribution function can be visualized by looking at the projection of $g(\boldsymbol{r})$ on the xy (flow and shear-gradient) plane, as seen in figure 13(*a–d*) for several different $Ca_{G,eff}$. At large $Ca_{G,eff}$, the pair distribution function clearly shows the ellipsoidal shape of the deformed capsule with a much less defined and softer contact region. The deformation in figure 13(*b*) is very minor, yet the pair-distribution function shows a noticeable ellipsoidal shape, which highlights the impact of capsule deformation on particle interactions that exceeds the simple change in particle geometry. Also note

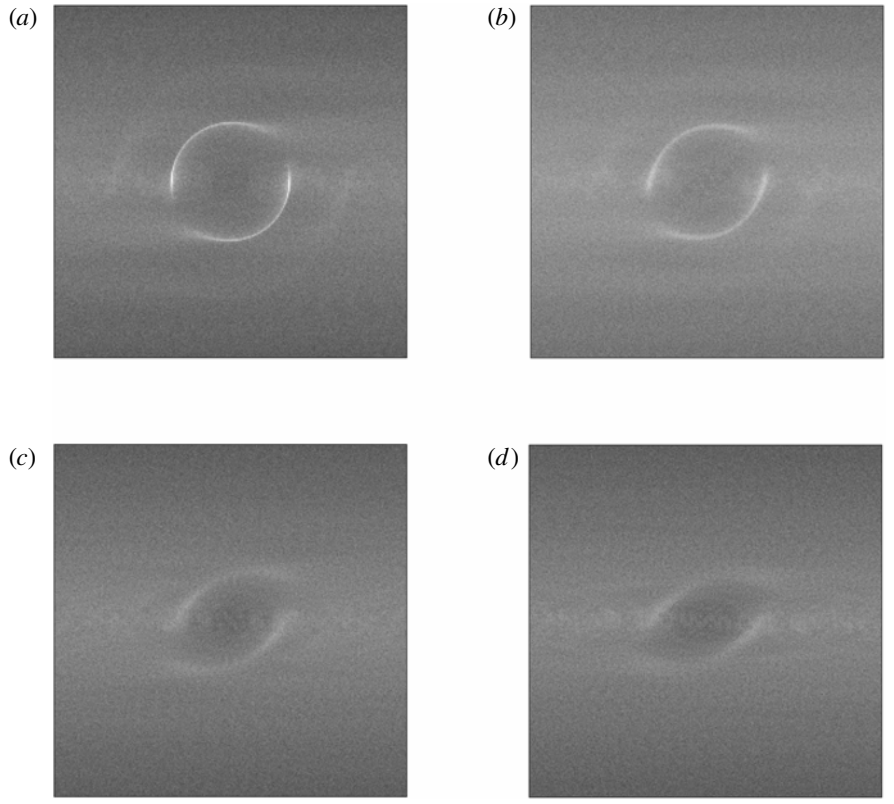

FIGURE 13. Projection of $g(\boldsymbol{r})$ in the xy plane for (*a*) $Ca_{G,eff} = 0.0$, (*b*) $Ca_{G,eff} = 0.01$, (*c*) $Ca_{G,eff} = 0.07$ and (*d*) $Ca_{G,eff} = 0.12$. All simulations are $\phi = 0.4$.

the slight appearance of bands aligned with the flow in the rigid and near-rigid cases. Such bands are not reported in SD simulations at these concentrations; however, order in suspension microstructure has been noted in simulations at higher concentrations (Morris & Katyal 2002; Sierou & Brady 2002). Experimentally, order has been seen in electrostatically stabilized suspensions (Chen, Ackerson & Zukoski 1994) suggesting that the relatively large interparticle force present in the LB/FE simulations may play a role.

The angular dependence of the pair-distribution function can be plotted for the LB/FE results; however, care must be taken to use a sufficiently sized radial range since the particle border is no longer spherical. Figure 14 shows the angular dependence for several $Ca_{G,eff}$, and a decrease in the asymmetry is seen at higher deformations. Note the high probability of finding another particle at $\theta = 0$ or $\theta = \pi$, which is indicative of particles forming a 'chain' in the flow direction. This result is not reported in SD simulations, but was noted in the LB simulations by Kulkarni & Morris (2008). Deformation reduces the impact of asymmetry in the particle configuration, including diminishing the probability of particle chains. Thus, the negative first normal stress difference seen in figure 9(*a*), which is generated via asymmetry in the pair-distribution function, relaxes as even minor levels of deformation are introduced. Stated another way, particle deformation tends to create softer interactions with larger gaps between particles, which reduces the impact of

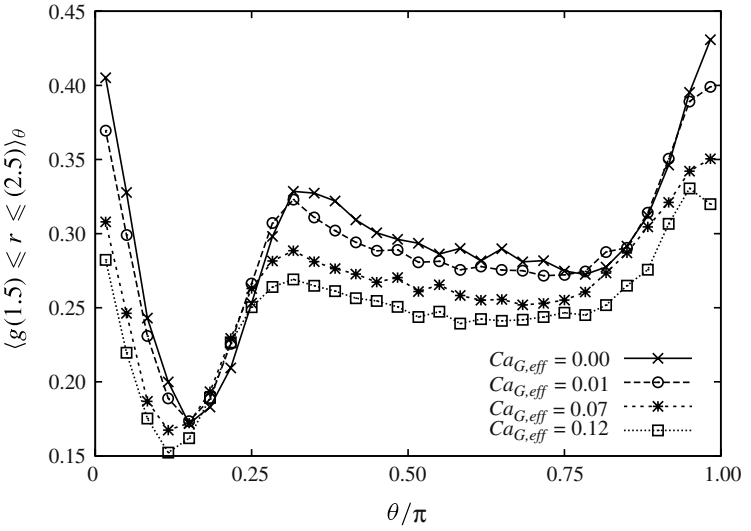

FIGURE 14. Angular dependence of pair distribution function for various Ca_G at $\phi = 0.4$. Reduced asymmetry reduces the impact of particle configuration on the rheology as deformation increases.

the configurational microstructure on the overall rheology. These effects, combined with the dilute-limit normal stress differences generated by the ellipsoidal shape of the deformed capsule (Clausen & Aidun 2010), cause the sign change in N_1 as the capillary number increases.

4.5. *Particle self-diffusion*

The study of diffusion and its connection to osmotic pressure has been widely studied for molecular and colloidal dispersions. In dilute colloidal suspensions, the thermal motion of the particles gives rise to a random walk and the well-known Stokes–Einstein result for the diffusivity, $D_0 = k_b T/6\pi\mu a$. In finite-volume-fraction suspensions, the self-diffusion is a function of the volume fraction, since interaction with neighbouring particles tends to inhibit particle mobility. For colloidal suspensions, the self-diffusion also has associated short- and long-time values, in which the short-time value corresponds to a random walk without significant interaction with neighbouring particles, and the long-time value corresponds to a random walk that includes interaction with neighbouring particles. The same fluctuation in the particle positions also gives rise to an osmotic pressure, which can be formulated via a minimization of free energy (Russel, Saville & Schowalter 1989) or rigourously connected to the fluctuating particle motion interacting via hydrodynamics (Brady 1993). Gradient-based or collective diffusion differs from self-diffusion; however, this phenomenon is also driven by the diffusive nature of the particle locations or alternately, as gradients in the osmotic pressure. Non-colloidal suspensions also demonstrate self-diffusion of the particles; however, particle diffusive behaviour is driven by interparticle interactions and not thermal motion. As has been demonstrated, this diffusive behaviour gives rise to a compressive particle pressure that is analogous to the osmotic pressure in a suspension of Brownian particles (Deboeuf *et al.* 2009).

Several LB/FE simulations have been performed for sufficient strains ($\dot{\gamma}t \sim 100$) to obtain a preliminary investigation of particle self-diffusion. Particle self-diffusion, like

$Ca_{G,eff}$	D_{yy}	D_{zz}
0.00	0.041	0.031
0.01	0.038	0.022
0.07	0.018	0.015
0.12	0.014	0.013

TABLE 2. Diffusion coefficients for simulations of 285 capsules at 40 % volume fraction.

any diffusive process, can be calculated by measuring the mean-squared displacements of the particle locations (Marchioro & Acrivos 2001; Sierou & Brady 2004), shown as

$$\langle \Delta y \Delta y \rangle \sim 2D_{yy}t, \tag{4.5}$$

where Δy is the y displacement and D_{yy} is the diffusion constant. A similar relationship holds for the z direction; however, the x direction diffusion must account for the affine displacements caused by the overall particle flow (Foss & Brady 1999; Sierou & Brady 2004). Diffusivities are made dimensionless by $\dot{\gamma}a^2$. The particle trajectories exhibits both short-and long-time behaviours. At times shorter than the time scale associated with particle interaction, particle trajectories are ballistic and the mean-squared displacements scale as t^2; at times significantly longer than the time scale associated with particle interaction, particle trajectories are diffusive and the mean-squared displacements scale as t. Previous studies into the self-diffusivity of non-colloidal suspensions of rigid spheres have shown that a large number of particles are required in order to achieve a reliable and convergent statistic for the diffusion tensor. The simulations in this paper, with 285 particles, are on the lower end of the required number of particles, thus any results for the diffusion will be subject to high levels of uncertainty. Nevertheless, several qualitative observations can be made about the magnitude of the diffusion coefficients as particle deformation is increased.

Figure 15(*a*,*b*) show the behaviour of the y and z mean-squared displacements. Calculating the slope in the long-time regime yields the diffusion coefficient from (4.5), and the results have been tabulated in table 2. For comparison, Sierou & Brady (2004) obtain diffusion coefficients of $D_{yy} = 0.0620 \pm 0.0060$ and $D_{zz} = 0.0290 \pm 0.0030$ for 40 % volume fraction rigid spheres. More accurate results from the LB/FE method will require more particles and ensemble averaging of many particle configurations. For all simulations, deformation caused a decrease in particle diffusivity, and $D_{yy} \leqslant D_{zz}$. Measurements of particle self-diffusivity are difficult to perform experimentally; however, researchers have reported some success (Leighton & Acrivos 1987; Breedveld *et al.* 2001*a*,*b*, 2002; Eckstein, Bailey & Shapiro 2006). Large variations in the reported diffusivity exist in literature making quantitative comparisons difficult. Much of the deviation in experimental results has been attributed to the short times measured, less than 10 strain units in most cases (Sierou & Brady 2004). This time, as seen in figure 15(*a*,*b*), is still within the transition region before true diffusive behaviour has been established.

Several trends exist: first, the diffusion is anisotropic, which is to be expected given the non-equilibrium microstructure and anisotropic normal stresses found in non-colloidal suspensions. The connection between normal stresses and particle diffusion can be seen by looking at the relative magnitudes of the diffusion and normal stresses in the shear-gradient and vorticity directions, where $|\Sigma^p_{22}| > |\Sigma^p_{33}|$ as $D_{yy} > D_{zz}$. Second, the time scale corresponding to the onset of diffusive behaviour does not seem to be

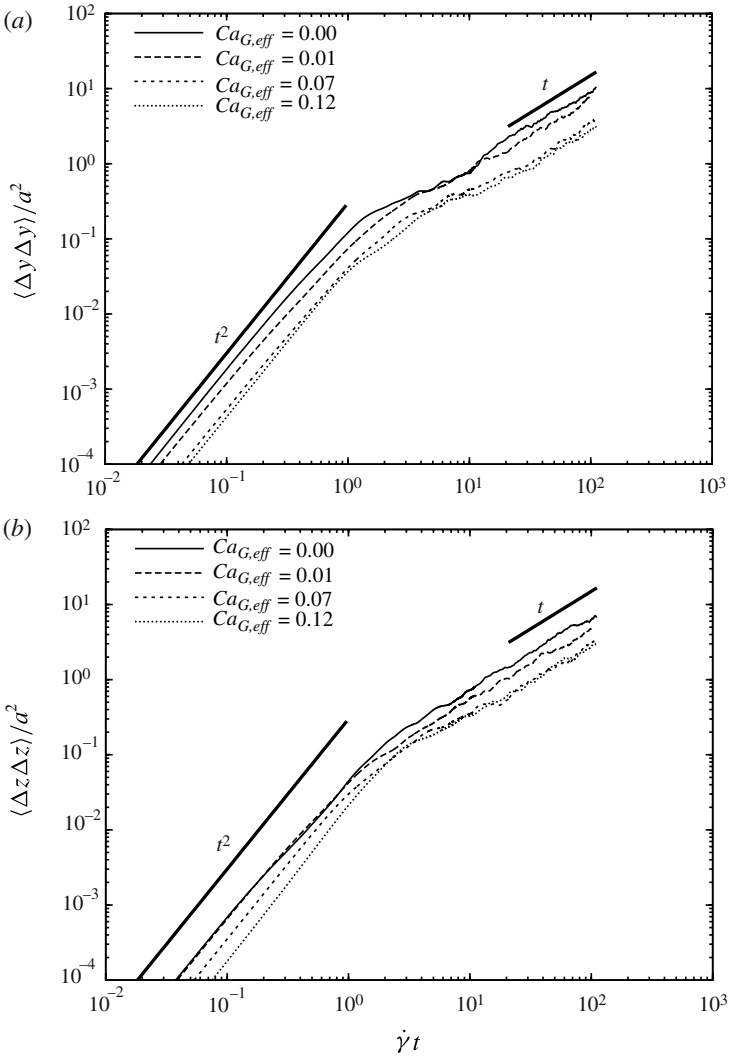

FIGURE 15. Mean-squared displacements of the particle position as a function of time for (*a*) the shear-gradient direction (y) and the (*b*) the vorticity direction (z). At long time scales particles show linear growth of displacement variance in contrast to the short time quadratic growth.

significantly affected by the level of deformation, which is to be expected since the time scale of particle deformation is significantly less than the time scale of diffusive behaviour. Finally, the deformation of the particles has a notable effect on diffusion. Mechanistically, this results from the modification of the interparticle interactions. In general, deformation decreases the observed diffusivity of the particles, which is also corroborated by the decreasing particle normal stress magnitudes shown in figure 7.

5. Conclusions

The rheology and microstructure of suspensions of initially spherical elastic capsules have been studied using a coupled LB/FE method. This method has been published

previously and used to study the effective viscosity of suspensions of red blood cells and capsules, as well as the dynamics and microstructure of isolated capsules. This method allows for the direct numerical simulation of dense capsule suspensions in a periodic domain under homogeneous shear, from which it is possible to calculate both suspension microstructure and rheology. Care must be taken when applying the LB method to capsule suspensions, particularly when investigating isotropic pressure contributions, due to the pseudo-compressible nature of the LB method and the mixing of fluids internal and external to the capsules. Simulations in the rigid limit agree well with existing literature for suspensions of rigid spheres, including the accurate resolution of the normal stresses. As the capsule's deformation is increased, the suspensions are found to be shear thinning, a result that is in agreement with the dilute-limit behaviour; however, the shear-thinning effect is more pronounced in dense suspensions owing to the impact of deformation on interparticle interactions.

In dense suspensions of rigid spherical particles, normal stresses are found to be compressive owing to asymmetry in the particle distribution function, i.e. there is an increased likelihood of finding neighbouring particles aligned along the compressional axis. As deformation is introduced, the overall tensile forces associated with deforming the capsule into an ellipsoidal shape drive a sign change in the first normal stress difference. In general, normal stresses are found to be more tensile in nature, which is seen as a large decrease in the isotropic particle pressure term of the particle-phase stress. The reduction in the compressive nature of the particle normal stresses corresponds with a reduction in particle self-diffusion. The self-diffusion shows a notable anisotropy, which is to be expected given the significantly anisotropic nature of the normal stresses. Larger simulations are needed to resolve the full self-diffusion tensor. The impact of the tensile particle stresses found in the flow direction diffusion coefficient would be interesting to study, as would the broad topic of collective diffusion (migration).

The average shear stress in the suspension largely dictates the single-body microstructure. The impact of changes in concentration to the capsule's orientation and deformation is minimal once accounting for the increased suspension viscosity, although a slight effect is seen. This suggests that the influence of capsule deformation on interparticle interactions and the configuration of the capsules with respect to one another plays a large role in shaping the rheology, especially at higher concentrations. The effect of interparticle interactions is highlighted by plotting the average stresslet value, which shows the per-particle contribution to the suspension rheology. Large changes in the average stresslet are noted at different concentrations, as expected from rigid suspension results, and altering the deformation of the particles also has a large effect on the average stresslet values. The behaviour of the average stresslet as deformation is introduced is markedly different at various concentrations, which means that the primary influence of deformation at moderate capillary numbers is not a dilute-limit effect but an alteration to the interparticle interactions. An attempt is made to quantify the configurational microstructure by measuring the pair distribution function with the caveat that the location of the particle border varies with deformation. Thus, a large radial range is used, and in general particle deformation results in less anisotropy in $g(\boldsymbol{r})$. Deformation results in larger gaps between particles and a more homogeneous distribution, which can also be seen in the projections of the pair distribution function. Perhaps a more useful statistic to investigate in the future would be the separation gap between particles, rather than the distance between particle centres.

This research was supported in part by the National Science Foundation through TeraGrid resources under grant number TG-CTS100012. Funding for J.R.C. was made available through the Institute of Paper Science and Technology at the Georgia Institute of Technology. D.A.R. was funded by the US Department of Defense through the American Society of Engineering Excellence SMART fellowship.

REFERENCES

ACRIVOS, A., MAURI, R. & FAN, X. 1993 Shear-induced resuspension in a Couette device. *Intl J. Multiphase Flow* **19** (5), 797–802.

AIDUN, C. K. & CLAUSEN, J. R. 2010 The lattice-Boltzmann method for complex flows. *Annu. Rev. Fluid Mech.* **42** (1), 439–472.

AIDUN, C. K. & LU, Y. 1995 Lattice Boltzmann simulation of solid particles suspended in fluid. *J. Stat. Phys.* **81** (1), 49–61.

AIDUN, C. K., LU, Y. & DING, E. J. 1998 Direct analysis of particulate suspensions with inertia using the discrete Boltzmann equation. *J. Fluid Mech.* **373**, 287–311.

BAGCHI, P. 2007 Mesoscale simulation of blood flow in small vessels. *Biophys. J.* **92** (6), 1858–1877.

BAGCHI, P. & KALLURI, R. M. 2010 Rheology of a dilute suspension of liquid-filled elastic capsules. *Phys. Rev.* E **81**, 056320.

BARTHÈS-BIESEL, D. 1980 Motion of a spherical microcapsule freely suspended in a linear shear flow. *J. Fluid Mech.* **100** (04), 831–853.

BARTHÈS-BIESEL, D. 2009 Capsule motion in flow: deformation and membrane buckling. *C. R. Physique* **10** (8), 764–774.

BARTHÈS-BIESEL, D. & RALLISON, J. M. 1981 The time-dependent deformation of a capsule freely suspended in a linear shear flow. *J. Fluid Mech.* **113**, 251–267.

BATCHELOR, G. K. 1970 The stress system in a suspension of force-free particles. *J. Fluid Mech.* **41**, 545–570.

BATCHELOR, G. K. & GREEN, J. T. 1972 The determination of the bulk stress in a suspension of spherical particles to order c^2. *J. Fluid Mech.* **56** (03), 401–427.

BHATNAGAR, P. L., GROSS, E. P. & KROOK, M. 1954 A model for collision processes in gases. I. Small amplitude processes in charged and neutral one-component systems. *Phys. Rev.* **94** (3), 511–525.

BIBEN, T. & MISBAH, C. 2003 Tumbling of vesicles under shear flow within an advected-field approach. *Phys. Rev.* E **67** (3), 031908.

BRADY, J. F. 1993 Brownian motion, hydrodynamics, and the osmotic pressure. *J. Chem. Phys.* **98** (4), 3335–3341.

BRADY, J. F. & BOSSIS, G. 1988 Stokesian Dynamics. *Annu. Rev. Fluid Mech.* **20** (1), 111–157.

BRADY, J. F. & MORRIS, J. F. 1997 Microstructure of strongly sheared suspensions and its impact on rheology and diffusion. *J. Fluid Mech.* **348**, 103–139.

BREEDVELD, V., VAN DEN ENDE, D., BOSSCHER, M., JONGSCHAAP, R. J. J. & MELLEMA, J. 2001*b* Measuring shear-induced self-diffusion in a counterrotating geometry. *Phys. Rev.* E **63** (2), 21403.

BREEDVELD, V., VAN DEN ENDE, D., BOSSCHER, M., JONGSCHAAP, R. J. J. & MELLEMA, J. 2002 Measurement of the full shear-induced self-diffusion tensor of noncolloidal suspensions. *J. Chem. Phys.* **116** (23), 10529–10535.

BREEDVELD, V., VAN DEN ENDE, D., JONGSCHAAP, R. J. J. & MELLEMA, J. 2001*b* Shear-induced diffusion and rheology of noncolloidal suspensions: time scales and particle displacements. *J. Chem. Phys.* **114** (13), 5923.

CHEN, L. B., ACKERSON, B. J. & ZUKOSKI, C. F. 1994 Rheological consequences of microstructural transitions in colloidal crystals. *J. Rheol.* **38**, 193–216.

CHEN, S. & DOOLEN, G. D. 1998 Lattice Boltzmann method for fluid flows. *Annu. Rev. Fluid Mech.* **30** (1), 329–364.

CLAUSEN, J. R. 2010 The effect of particle deformation on the rheology and microstructure of noncolloidal suspensions. PhD thesis, Georgia Institute of Technology.

CLAUSEN, J. R. & AIDUN, C. K. 2009 Galilean invariance in the lattice-Boltzmann method and its effect on the calculation of rheological properties in suspensions. *Intl J. Multiphase Flow* **35**, 307–311.

CLAUSEN, J. R. & AIDUN, C. K. 2010 Capsule dynamics and rheology in shear flow: particle pressure and normal stress. *Phys. Fluids* **22**, 123302.

CLAUSEN, J. R., REASOR, D. A. & AIDUN, C. K. 2010 Parallel performance of a lattice-Boltzmann/finite element cellular blood flow solver on the IBM Blue Gene/P architecture. *Comput. Phys. Commun.* **181** (6), 1013–1020.

COUPIER, G., KAOUI, B., PODGORSKI, T. & MISBAH, C. 2008 Noninertial lateral migration of vesicles in bounded Poiseuille flow. *Phys. Fluids* **20**, 111702.

DANKER, G. & MISBAH, C. 2007 Rheology of a dilute suspension of vesicles. *Phys. Rev. Lett.* **98** (8), 088104.

DEBOEUF, A., GAUTHIER, G., MARTIN, J., YURKOVETSKY, Y. & MORRIS, J. F. 2009 Particle pressure in a sheared suspension: a bridge from osmosis to granular dilatancy. *Phys. Rev. Lett.* **102** (10), 108301.

DING, E. J. & AIDUN, C. K. 2003 Extension of the lattice-Boltzmann method for direct simulation of suspended particles near contact. *J. Stat. Phys.* **112** (3), 685–708.

DUPIN, M. M., HALLIDAY, I., CARE, C. M., ALBOUL, L. & MUNN, L. L. 2007 Modeling the flow of dense suspensions of deformable particles in three dimensions. *Phys. Rev.* E **75** (6), 66707.

ECKSTEIN, E. C., BAILEY, D. G. & SHAPIRO, A. H. 2006 Self-diffusion of particles in shear flow of a suspension. *J. Fluid Mech.* **79** (01), 191–208.

EILERS, H. 1941 Die viskosität von emulsionen hochviskoser stoffe als funktion der konzentration. *Colloid Polym. Sci.* **97** (3), 313–321.

EINSTEIN, A. 1906 Zur Theorie der Brownschen Bewegung. *Ann. Phys. (Leipzig)* **19**, 371–381.

EINSTEIN, A. 1911 Berichtigung zu meiner Arbeit: eine neue Bestimmung der Moleküldimensionen. *Ann. Phys. (Leipzig)* **34** (3), 591–592.

FOSS, D. R. & BRADY, J. F. 1999 Self-diffusion in sheared suspensions by dynamic simulation. *J. Fluid Mech.* **401**, 243–274.

FRISCH, U., D'HUMIÈRES, D., HASSLACHER, B., LALLEMAND, P., POMEAU, Y. & RIVET, J.-P. 1987 Lattice gas hydrodynamics in two and three dimensions. *Complex Syst.* **1** (4), 649–707.

GADALA-MARIA, F. 1979 The rheology of concentrated suspensions. PhD thesis, Standford University.

GHIGLIOTTI, G., BIBEN, T. & MISBAH, C. 2010 Rheology of a dilute two-dimensional suspension of vesicles. *J. Fluid Mech.* **653**, 489–518.

GINZBOURG, I. & ADLER, P. M. 1994 Boundary flow condition analysis for the 3-dimensional lattice Boltzmann model. *J. Phys.* II **4** (2), 191–214.

GODDARD, J. D. & MILLER, C. 1967 Nonlinear effects in the rheology of dilute suspensions. *J. Fluid Mech.* **28** (04), 657–673.

HIGUERA, F. J. & JIMENEZ, J. 1989 Boltzmann approach to lattice gas simulations. *Europhys. Lett.* **9** (7), 663–668.

HINCH, E. J. & LEAL, L. G. 1972 The effect of Brownian motion on the rheological properties of a suspension of non-spherical particles. *J. Fluid Mech.* **52** (04), 683–712.

HINCH, E. J. & LEAL, L. G. 1973 Time-dependent shear flows of a suspension of particles with weak Brownian rotations. *J. Fluid Mech.* **57** (04), 753–767.

D'HUMIÈRES, D., GINZBURG, I., KRAFCZYK, M., LALLEMAND, P. & LUO, L.-S. 2002 Multiple-relaxation-time lattice Boltzmann models in three dimensions. *Phil. Trans. R. Soc. Lond.* A **360** (1792), 437–451.

JEFFREY, D. J., MORRIS, J. F. & BRADY, J. F. 1993 The pressure moments for two rigid spheres in low-Reynolds-number flow. *Phys. Fluids* A **5** (10), 2317–2325.

JUNK, M. & YONG, W. A. 2003 Rigorous Navier–Stokes limit of the lattice Boltzmann equation. *Asymptotic Anal.* **35** (2), 165–185.

KAOUI, B., RISTOW, G. H., CANTAT, I., MISBAH, C. & ZIMMERMANN, W. 2008 Lateral migration of a two-dimensional vesicle in unbounded Poiseuille flow. *Phys. Rev.* E **77** (2), 21903.

KARNIS, A. & MASON, S. G. 1967 Particle motions in sheared suspensions XXIII. Wall migration of fluid drops. *J. Colloid Interface Sci.* **24** (2), 164–169.

KELLER, S. R. & SKALAK, R. 1982 Motion of a tank-treading ellipsoidal particle in a shear flow. *J. Fluid Mech.* **120**, 27–47.

KENNEDY, M. R., POZRIKIDIS, C. & SKALAK, R. 1994 Motion and deformation of liquid drops, and the rheology of dilute emulsions in simple shear flow. *Comput. Fluids* **23** (2), 251–278.

KRIEGER, I. M. & DOUGHERTY, T. J. 1959 A mechanism for non-Newtonian flow in suspensions of rigid spheres. *J. Rheol.* **3** (1), 137–152.

KULKARNI, P. M. & MORRIS, J. F. 2008 Suspension properties at finite Reynolds number from simulated shear flow. *Phys. Fluids* **20** (4), 040602.

LAC, E., BARTHÈS-BIESEL, D., PELEKASIS, N. A. & TSAMOPOULOS, J. 2004 Spherical capsules in three-dimensional unbounded Stokes flows: effect of the membrane constitutive law and onset of buckling. *J. Fluid Mech.* **516**, 303–334.

LADD, A. J. C. 1994*a* Numerical simulations of particulate suspensions via a discretized Boltzmann equation. Part 1. Theoretical foundation. *J. Fluid Mech.* **271**, 285–309.

LADD, A. J. C. 1994*b* Numerical simulations of particulate suspensions via a discretized Boltzmann equation. Part 2. Numerical results. *J. Fluid Mech.* **271**, 311–339.

LADD, A. J. C. & VERBERG, R. 2001 Lattice-Boltzmann simulations of particle–fluid suspensions. *J. Stat. Phys.* **104** (5), 1191–1251.

LEIGHTON, D. T. & ACRIVOS, A. 1987 The shear-induced migration of particles in concentrated suspensions. *J. Fluid Mech.* **181**, 415–439.

LIN, C. J., PEERY, J. H. & SCHOWALTER, W. R. 1970 Simple shear flow round a rigid sphere: inertial effects and suspension rheology. *J. Fluid Mech.* **44** (01), 1–17.

LOEWENBERG, M. & HINCH, E. J. 1996 Numerical simulation of a concentrated emulsion in shear flow. *J. Fluid Mech.* **321**, 395–419.

LORENZ, E., CAIAZZO, A. & HOEKSTRA, A. G. 2009 Corrected momentum exchange method for lattice Boltzmann simulations of suspension flow. *Phys. Rev.* E **79** (3), 036705.

MACMECCAN, R. M. 2007 Mechanistic effects of erythrocytes on platelet deposition in coronary thrombosis. PhD thesis, Georgia Institute of Technology.

MACMECCAN, R. M., CLAUSEN, J. R., NEITZEL, G. P. & AIDUN, C. K. 2009 Simulating deformable particle suspensions using a coupled lattice-Boltzmann and finite-element method. *J. Fluid Mech.* **618**, 13–39.

MARCHIORO, M. & ACRIVOS, A. 2001 Shear-induced particle diffusivities from numerical simulations. *J. Fluid Mech.* **443**, 101–128.

MCNAMARA, G. R. & ZANETTI, G. 1988 Use of the Boltzmann equation to simulate lattice-gas automata. *Phys. Rev. Lett.* **61** (20), 2332–2335.

MEWIS, J., FRITH, W. J., STRIVENS, T. A. & RUSSEL, W. B. 1989 The rheology of suspensions containing polymerically stabilized particles. *AIChE J.* **35** (3), 415–422.

MISBAH, C. 2006 Vacillating breathing and tumbling of vesicles under shear flow. *Phys. Rev. Lett.* **96** (2), 028104.

MORRIS, J. F. & BOULAY, F. 1999 Curvilinear flows of noncolloidal suspensions: the role of normal stresses. *J. Rheol.* **43** (5), 1213–1237.

MORRIS, J. F. & BRADY, J. F. 1998 Pressure-driven flow of a suspension: Buoyancy effects. *Intl J. Multiphase Flow* **24** (1), 105–130.

MORRIS, J. F. & KATYAL, B. 2002 Microstructure from simulated Brownian suspension flows at large shear rate. *Phys. Fluids* **14** (6), 1920–1937.

NOBLE, D. R., CHEN, S., GEORGIADIS, J. G. & BUCKIUS, R. O. 1995 A consistent hydrodynamic boundary condition for the lattice Boltzmann method. *Phys. Fluids* **7** (1), 203–209.

NOTT, P. R. & BRADY, J. F. 1994 Pressure-driven suspension flow: simulation and theory. *J. Fluid Mech.* **275**, 157–199.

NOURGALIEV, R. R., DINH, T. N., THEOFANOUS, T. G. & JOSEPH, D. 2003 The lattice Boltzmann equation method: theoretical interpretation, numerics and implications. *Intl J. Multiphase Flow* **29** (1), 117–169.

PAPIR, Y. S. & KRIEGER, I. M. 1970 Rheological studies on dispersions of uniform colloidal spheres II. Dispersions in nonaqueous media. *J. Colloid. Interface Sci.* **34** (1), 126–130.

PARSI, F. & GADALA-MARIA, F. 1987 Fore-and-aft asymmetry in a concentrated suspension of solid spheres. *J. Rheol.* **31** (8), 725–732.

PHUNG, T. N., BRADY, J. F. & BOSSIS, G. 1996 Stokesian dynamics simulation of Brownian suspensions. *J. Fluid Mech.* **313**, 181–207.

RAMANUJAN, S. & POZRIKIDIS, C. 1998 Deformation of liquid capsules enclosed by elastic membranes in simple shear flow: large deformations and the effect of fluid viscosities. *J. Fluid Mech.* **361**, 117–143.

REASOR, D. A., CLAUSEN, J. R. & AIDUN, C. K. 2011 Coupling the lattice-Boltzmann and spectrin-link methods for the direct numerical simulation of cellular blood flow. *Intl J. Numer. Meth. Fluids*, doi:10.1002/fld.2534.

ROSCOE, R. 1967 On the rheology of a suspension of viscoelastic spheres in a viscous liquid. *J. Fluid Mech.* **28** (02), 273–293.

RUSSEL, W. B., SAVILLE, D. A. & SCHOWALTER, W. R. 1989 *Colloidal Dispersions*. Cambridge University Press.

SIEROU, A. & BRADY, J. F. 2001 Accelerated Stokesian dynamics simulations. *J. Fluid Mech.* **448**, 115–146.

SIEROU, A. & BRADY, J. F. 2002 Rheology and microstructure in concentrated noncolloidal suspensions. *J. Rheol.* **46**, 1031–1056.

SIEROU, A. & BRADY, J. F. 2004 Shear-induced self-diffusion in non-colloidal suspensions. *J. Fluid Mech.* **506**, 285–314.

SINGH, A. & NOTT, P. R. 2003 Experimental measurements of the normal stresses in sheared Stokesian suspensions. *J. Fluid Mech.* **490**, 293–320.

STICKEL, J. J. & POWELL, R. L. 2005 Fluid mechanics and rheology of dense suspensions. *Annu. Rev. Fluid Mech.* **37** (01), 129–149.

SUKUMARAN, S. & SEIFERT, U. 2001 Influence of shear flow on vesicles near a wall: a numerical study. *Phys. Rev.* E **64** (1), 11916.

TAYLOR, G. I. 1932 The viscosity of a fluid containing small drops of another fluid. *Proc. R. Soc. Lond.* A **138** (834), 41–48.

VAHALA, G., KEATING, B., SOE, M., YEPEZ, J., VAHALA, L. & ZIEGELER, S. 2009 Entropic, LES and boundary conditions in lattice Boltzmann simulations of turbulence. *Eur. Phys. J. Special Topics* **171** (1), 167–171.

VLAHOVSKA, P. M. & GRACIA, R. S. 2007 Dynamics of a viscous vesicle in linear flows. *Phys. Rev.* E **75** (1), 016313.

WAGNER, A. J. & PAGONABARRAGA, I. 2002 Lees–Edwards boundary conditions for lattice Boltzmann. *J. Stat. Phys.* **107** (1), 521–537.

WU, J. & AIDUN, C. K. 2009 Simulating 3D deformable particle suspensions using lattice Boltzmann method with discrete external boundary force. *Intl J. Numer. Meth. Fluids* **62** (7), 765–783.

WU, J. & AIDUN, C. K. 2010 A method for direct simulation of flexible fiber suspensions using lattice-Boltzmann equation with external boundary force. *Intl J. Multiphase Flow* **36**, 202–209.

YURKOVETSKY, Y. & MORRIS, J. F. 2008 Particle pressure in sheared Brownian suspensions. *J. Rheol.* **52** (1), 141–164.

ZARRAGA, I. E., HILL, D. A. & LEIGHTON, D. T. 2000 The characterization of the total stress of concentrated suspensions of noncolloidal spheres in Newtonian fluids. *J. Rheol.* **44** (2), 185–220.

ZHANG, J., JOHNSON, P. C. & POPEL, A. S. 2007 An immersed boundary lattice Boltzmann approach to simulate deformable liquid capsules and its application to microscopic blood flows. *Phys. Biol.* **4**, 285.

ZINCHENKO, A. Z. & DAVIS, R. H. 2002 Shear flow of highly concentrated emulsions of deformable drops by numerical simulations. *J. Fluid Mech.* **455**, 21–62.